

1 **TITLE**

2 Ultraviolet-Visible Diffuse Reflectance Spectroscopy (UV-Vis DRS), a rapid and non-destructive
3 analytical tool for the identification of Saharan dust events in Particulate Matter filters

4

5 **AUTHORS**

6

7 Pietro Morozzi ^a

8 Barbara Ballarin ^b

9 Sara Arcozzi ^c

10 Erika Brattich ^d

11 Franco Lucarelli ^e

12 Silvia Nava ^e

13 Pedro J. Gómez-Cascales ^f

14 Jose A. G. Orza ^f

15 Laura Tositti ^a

16

17 ^a Department of Chemistry “G. Ciamician”, University of Bologna, Via Selmi, 2, 40126 Bologna,
18 Italy

19 ^b Department of Industrial Chemistry Toso Montanari, University of Bologna, Viale del
20 Risorgimento, 4, 40136 Bologna, Italy

21 ^c Department of Industrial Chemistry Toso Montanari, University of Bologna, Via Granarolo, 62,
22 48018 Faenza, Italy

23 ^d Department of Physics and Astronomy, University of Bologna, Via Irnerio, 46, 40126 Bologna,
24 Italy

25 ^e Department of Physics and Astronomy, University of Florence and National Institute of Nuclear
26 Physics (INFN), Florence Section, Via Sansone, 1, 50019 Sesto Fiorentino, Italy

27 ^f SCOLAb, Department of Applied Physics, University Miguel Hernandez de Elche, 03202 Elche,
28 Spain

29

30 ***Corresponding author:** Pietro Morozzi

31 e-mail address: pietro.morozzi2@unibo.it

32 mailing address: Via Selmi 2, 40126 Bologna (ITALY)

1. INTRODUCTION

33
34 Mineral dust uplifted into the troposphere by turbulence and wind in the North African desert is often
35 transported across thousands of kilometers including the Mediterranean basin, the European continent
36 sometimes up to the northernmost countries and/or the American continent, according to the season
37 (e.g., Middleton & Goudie, 2002). Overall the Mediterranean basin owing to proximity and average
38 circulation patterns, is directly and frequently affected by the so called Saharan dust incursions
39 throughout the year with events whose intensity and frequency are object of extensive research
40 (Brattich et al., 2015a; Brattich et al., 2015b; Cabello et al., 2016; Cuevas et al., 2017; Cusack et al.,
41 2012; Israelevich et al., 2012; Riccio et al., 2009; Tositti et al., 2014). This occurrence is being
42 reported as increasing in likely connection with global warming (Middleton & Goudie, 2002;
43 Soleimani et al., 2020). These events have often been linked with PM₁₀ exceedances in respect to EU
44 air quality standards drawing attention on potential health hazards as well as on their correct
45 management (Diapouli et al., 2017; Krasnov et al., 2014; Matassoni et al., 2011; Nava et al., 2012;
46 Querol et al., 2019). The current EU Air Quality standards for PM₁₀ are far less stringent than the
47 WHO standards with a threshold of 20 µg/m³ (WHO annual mean) vs. a 40 µg/m³ for the former
48 (WHO, 2006). It is to note that the EU regulation allows to eliminate from the annual inventory of
49 exceedances the natural events such as Saharan dust incursions thus improving the overall
50 environmental performance for this parameter (EEA, 2012).

51 Saharan dust does not only affect air quality standards, but plays a significant role in climate change
52 by direct and indirect effect, the former by modifying the optical properties of the troposphere (e.g.,
53 Chin et al., 2009; Ginoux, 2017; IDSO, 1981; Littmann & Steinrücke, 1989; Sokolik & Toon, 1999),
54 while the latter is associated with cloud processing and nucleation (see for example Reicher et al.,
55 2019). Furthermore, mineral dust strongly influences the atmospheric reactivity through complex
56 surface chemical reactions (Usher et al., 2003). Saharan dust transport is also connected with adverse

57 health effects and increase in the mortality rate among the Mediterranean population (Karanasiou et
58 al., 2012; Querol et al., 2019; Stafoggia et al., 2016).

59 Mineral particles may also affect the oxidant capacity of the troposphere by catalyzing ozone
60 destruction, an important pollutant and reactive greenhouse gas (Bonasoni et al., 2003; Dickerson et
61 al., 1997; Prospero et al., 1995). Moreover, iron contained in Saharan dust plumes can settle on
62 oceanic surfaces and behave as a nutrient for marine phytoplankton, with beneficial outcome for
63 oligotrophic aquatic systems, but potentially damaging the eutrophic ones (e.g., Bristow et al., 2010;
64 Molinaroli & Masiol, 2006). However, Saharan dust has been often associated with a coral decline in
65 the Caribbean region, suggesting that either mineral or microbiological components of Saharan dust
66 may reveal detrimental to fragile ecosystems (Garrison et al., 2003; Shinn et al., 2000).

67 The complex role and behavior of mineral dust from Saharan regions, as briefly outlined, clearly
68 shows the importance of identifying its occurrence in a given airshed in a simple, fast and unambiguous
69 way. Common procedures to identify dust outbreaks may use a combination of back-trajectory
70 analysis, satellite retrievals, and the output of dust prediction models. Collectively they provide a
71 reasonable degree of evidence though each of these tools has limitations: a back-trajectory travelling
72 over North Africa is not always associated to dust advection; satellite retrievals are limited by cloud
73 coverage and transit time; uncertainties in dust model estimates remain, due to incomplete
74 representation of several processes. Moreover, though meteorological forecasts are presently very
75 well evolved enabling a timely Saharan dust alerting, most efforts are mainly retrospective and used
76 for confirmation of more focused experimental activities from Lidar experiments and remote sensing
77 to aerosol chemical speciation, preventing an efficient Saharan dust diagnosis (Pérez et al., 2011;
78 Spyrou et al., 2010). All of this information is frequently combined with PM₁₀ levels or columnar
79 aerosol properties at the study site. These levels are compared with local threshold values or
80 background levels obtained by their own time series (Barnaba et al., 2017) or with PM₁₀
81 concentrations at a close regional background site (EC Commission, 2011; Escudero et al., 2007).

82 Saharan mineral dust consists mainly of silicates, aluminum oxides, carbonates, gypsum, and iron
83 oxides, with a specific composition that depends on the geological material from its lifting place (e.g.,
84 Linke et al., 2006). Chemical speciation analysis is largely used to characterize aerosol composition
85 as a function of its sources. Mineral dust is successfully identified with all the basic techniques
86 devoted to elemental inorganic analysis; X-ray emission techniques such as Particle Induced X-ray
87 Emission (PIXE) and X-ray fluorescence (XRF) are the most efficient and non-destructive ones since
88 they allow a prompt detection of the abundant lithogenic components, without any demanding and
89 costly chemical processing in advance. Crustal elements like silicon (Si), aluminum (Al), titanium
90 (Ti), calcium (Ca), and iron (Fe) are successfully used to identify Saharan dust events, as reported by,
91 e.g., Alastuey et al., 2016; Formenti et al., 2010; Marconi et al., 2014; Nava et al., 2012; Rodríguez
92 et al., 2020. In most cases, elemental analysis is complemented by ion chromatography wherein the
93 most informative species associated with mineral dust is calcium ion (Ca^{2+}) (Escudero et al., 2005;
94 Flentje et al., 2015; Putaud et al., 2004). This approach can be integrated by the detection of mineral
95 species such as quartz, feldspars, illite, smectite, kaolinite, chlorite, vermiculite, mica, calcite,
96 gypsum, hematite and goethite (Caquineau et al., 2002; Journet et al., 2014) requiring X-Ray
97 Diffraction (XRD) (Menéndez et al., 2007; Shao et al., 2007), and Scanning Electron Microscopy
98 (SEM) (Menéndez et al., 2007; Remoundaki et al., 2011). However, many of these analytical
99 techniques are expensive, time consuming, and require sophisticated instrumental facilities and
100 highly skilled personnel. Furthermore, X-ray emission and diffraction techniques are not routinely
101 adopted by the Environmental Protection Agencies, at least in Europe, where, as required by Air
102 Quality regulation, chemical speciation of PM_{10} is typically based on ion chemistry and on a very
103 limited selection of pollutants including, beside benzo-a-pyrene normalized PAH's, only a few trace
104 elements in most cases requiring wet chemical pre-treatment followed by Atomic Absorption or
105 Inductively Coupled Plasma Spectroscopies (EU, 2008).

106 In this work, a procedure based exclusively on Ultraviolet-Visible Diffuse Reflectance Spectroscopy
107 (UV-Vis DRS) (Torrent & Barrón, 2008) is proposed as a simple, cheap, efficient, rapid, and non-
108 destructive analysis of particulate samples collected on a membrane for Saharan Dust transport
109 diagnosis. This method is based on the integrated use of aerosol mass load data and the detection of
110 iron oxides, which account for approximately 2 to 7 % in weight of the total amount of mineral dust
111 (Alfaro et al., 2004; Formenti et al., 2008; Goudie et al., 2006) in atmospheric aerosol. Differently
112 from most crustal materials and in spite of comparable concentration range, iron oxides in Saharan
113 Dust mainly consist of goethite (predominant, 52-78% of the total iron oxides) and hematite (22-48
114 % of the total iron oxides) (Formenti et al., 2014; Shi et al., 2012; Lafon et al., 2006). Since these
115 minerals are important markers of mineral dust (Formenti et al., 2014; Lafon et al., 2006; Shi et al.,
116 2012), they can be used as proxies for Saharan dust events in locations characterized by a low
117 background of iron oxides from other more common sources, i.e. the Earth's crust especially by soil
118 resuspension or technogenic ones such as metal works. Hematite and goethite are typically
119 characterized by intense color shades, which can impart a yellowish to red tone to atmospheric dust
120 particles (Arimoto et al., 2002). The proposed methodology is characterized by: (a) color metrological
121 parametrization and (b) iron mineral oxides semi-quantification of the analyzed PM filters, followed
122 by (c) chemometric tools. It can be integrated into routine sampling when no further speciation
123 analysis is needed. This procedure therefore can be deemed as a cheap but robust screening test
124 enabling to associate high PM₁₀ values with a measurable and reliable Saharan dust tracer.

125

126 **2. MATERIALS AND METHODS**

127 The Materials and Methods section is organized as follows:

128 (a) Subsection 2.1 describes the PM₁₀ samples used for the application and characterization of the
129 UV-Vis DRS methodology reported in this work;

130 (b) Subsection 2.2 describes in detail the method used, paying particular attention to the instrumental
131 configuration and analysis method of PM filters (subsection 2.2.1), how it is possible to parameterize
132 the colour of the analyzed filters (subsection 2.2.2) and obtain semi-quantitative data of iron oxide
133 minerals from sample reflectance spectra (subsection 2.2.3);

134 (c) Subsection 2.3 presents the validation of the proposed methodology. After checking the main
135 results of the proposed methodology (subsection 2.3.1), chemometric methods are used to identify
136 the PM filters that have been subjected to a Saharan dust transport event (subsection 2.3.2.1), and the
137 diagnosis obtained are assessed and confirmed by a residence time analysis of back-trajectory
138 ensembles (subsection 2.3.2.2).

139 **2.1 Particulate matter samples**

140 PM₁₀ samples analyzed in this work were collected at Sierra Nevada a high altitude site (37.096 N, -
141 3.387 W, 2550 m a.s.l.) in Southern Spain, within the framework of the Spanish national project
142 FRESA (Impact of dust-laden African air masses and of stratospheric air masses in the Iberian
143 Peninsula. Role of the Atlas Mountains, Ref: CGL2015-70741-R). The sampling station is located in
144 an area scarcely influenced by traffic and other anthropogenic sources, but strongly impacted by
145 Saharan dust incursion events due to its proximity to North Africa (Figure 1).

146 PM sampling was carried out using a high volume PM₁₀ sampler (CAV-A/mb, MCV S.A.) on a
147 weekly basis (168 h at 30 m³/h) using quartz filters (Ø 15 cm, Whatman QM-A quartz filters) from 8
148 June to 11 October 2016. Nineteen weekly PM₁₀ samples (labeled as SN1-SN19) were overall
149 obtained and processed along with three field blanks (labeled as B1-B3).

150 **2.2 The UV-Vis DRS methodology**

151 *2.2.1 Sample preparation and UV-Vis DRS analysis*

152 UV-Vis Diffuse Reflectance Spectroscopy is a widely used, basic spectrophotometric technique for
153 the analysis of powders and surfaces, requiring a negligible sample preparation (Torrent & Barrón,
154 2008). It is based on the surface dispersion of a fraction of the UV-Vis incident radiation on it. A UV-
155 Vis collimated light beam is directed with a certain angle onto the sample and, as a result, an ensemble
156 of optical processes leads to radiation reflection by the sample surface on the whole overlying
157 hemisphere. As a rule, the radiation reflected by a sample can be considered as the sum of two
158 components: regular (or specular) and diffuse (or nondirectional) reflectance (e.g., Torrent & Barrón,
159 2008). Regular reflectance occurs when incident radiation hits an ideally smooth and planar surface
160 (i.e. without roughness) of the sample, and it is then reflected at an angle equal to the angle of
161 incidence (Fresnel law). Instead, diffuse reflectance is a combination of several optical phenomena,
162 such as multiple reflections, scattering and refraction, which disperse the radiation at all of the angles
163 of the hemisphere of origin of the incident radiation (Blitz, 1998). Diffuse reflectance, which depends
164 on the physico-chemical properties and color of the surface, is therefore the most informative
165 component (Sellitto et al., 2008).

166 Diffuse reflectance spectroscopy of PM filters has been conducted with an ordinary UV-Vis
167 spectrophotometer (Perkin Elmer Lambda 35, UV-Vis range) equipped with an integrating sphere;
168 In this configuration all the reflected radiation emitted by the sample can be diffused and thereafter
169 efficiently analyzed by the inner walls of the integrating sphere. The analysis does not include any
170 sample chemical preparation: to the scope a square punch of 1.8 cm x 1.8 cm of a quartz PM filter is
171 placed inside a flat sample holder, designed to position the sample for beam irradiation at a 0°
172 incidence angle, and lodged over the reflectance sample port of the integrating sphere, a 50 mm
173 diameter Labsphere RSA-PE-20 (Labsphere, United States). With the 0° sample holder in place, any

174 specular component of reflection from the sample is excluded from measurement, since this
175 component is directed out of the sphere through the transmittance sample entrance port. This
176 integrating sphere configuration is named 0°/diffuse (0°/d) and Figure 2 shows its operating scheme.
177 Sample aliquots were carefully cut by means of a square die-cutting tool with a side of 1.8 cm. The
178 UV-Vis DRS analysis of the latter is non-destructive since the side containing the particulate material
179 is analyzed as it is, without any treatment and contact with the instrument. Firstly, a Spectralon white
180 standard (USRS-99-010-EPV, Labsphere, United States) was analyzed as a reference and the
181 instrumental autozero was performed. Then, one aliquot from each field blanks (B1-B3) was prepared
182 and B1 portion was used for the background correction. Subsequently, the analysis of the remaining
183 blank portions (B2 and B3) and the PM sampled filters was carried out. In particular, beside blanks,
184 three distinct replicates of each PM sampled filter were prepared and analyzed for statistical purposes
185 as well as to account for filter anisotropy. In this way, a total of 59 analyses were completed for this
186 work. Therefore, the percentage reflectance (% R), i.e. the ratio between the intensity of the radiation
187 reflected by the sample and the intensity of the total radiation reflected by a white diffuse reflectance
188 standard, was determined for each of the analyzed portions. In particular, this parameter was
189 measured as a function of the wavelength λ of the UV-Vis incident radiation (i.e., reflectance spectra
190 were obtained), based on the following instrumental parameters: λ range = 780 - 380 nm; resolution
191 = 0.3 nm; scan speed = 480 nm/min, smoothing = 2 nm, and slit = 2 nm.

192 *2.2.2 Color parametrization*

193 Aerosol sample color is measured by means of its UV-Vis reflectance spectrum. Indeed, sample color
194 strongly depends on its diffuse reflection: an object irradiated by a light source disperses part of the
195 incident radiation by diffuse reflection, which is subsequently collected by the eyes of an observer
196 which in turn act as transducers, converting the light signal into appropriate electrical impulses for
197 the brain. Ultimately, these impulses are integrated and processed by the latter, which generates the
198 color perception for the observer (Kremers et al., 2016). Therefore, color is an extremely complex

199 and subjective entity, as it is not a specific feature of the object itself, but depends on many variables
200 such as light source, optical behavior of the object, observer's eyes and brain, etc. Since 1931, the
201 International Commission on Illumination (CIE) has released guidelines to standardize color
202 perception, based on the definition of three elements: light source, observer, and colorimetric spaces.
203 The latter are mathematical models capable to define the color of an object in a rigorous manner
204 (Ibraheem et al., 2012). One of the most used colorimetric space is the CIE $L^*a^*b^*$ (CIELAB) (ISO-
205 CIE 11664-4-2019), which uses three cartesian components to uniquely define color sample: L^* ,
206 which indicates the CIELAB lightness in the range 0 (pure black) to 100 (pure white); a^* , measuring
207 the CIELAB redness-greenness coordinate; and b^* , associated with the CIELAB yellowness-blueness
208 coordinate. This colorimetric space can also be defined in polar coordinates, thus obtaining the CIE
209 $L^*C_{ab}^*h_{ab}^\circ$ space (CIELCH) (ISO-CIE 11664-4-2019), wherein: L^* indicates the CIELAB lightness;
210 C_{ab}^* represents the CIELAB chroma, a measure of the color intensity, defining to what extent a given
211 color shade is "contaminated" by gray; and h_{ab}° indicates the CIELAB hue angle, whose value is
212 expressed in degrees and describes the color tone. In particular, the 0° angle represents the red color.
213 Because of their easy interpretability, in this work the mathematical definition of the colors of the
214 analyzed portion samples was carried out employing the CIELAB and CIELCH spaces, starting from
215 the reflectance spectra obtained and using the Color 2.01 software (Perkin Elmer Ltd, United
216 Kingdom). Standard Illuminant D65 was set up as a representation of solar light source, according to
217 CIE (ISO-CIE 11664-2-2020), and an observer angle of 10° was set up with the aim of simulating the
218 average spectral response in human observers (ISO-CIE 11664-1-2019). Average values and the
219 standard deviations of the colorimetric parameters (L^* , a^* , b^* , C_{ab}^* , and h_{ab}°) were calculated for the
220 blank filter (B) and the 19 samples (SN1,...SN19). The CIELAB average data were used for color
221 visualization through the online tool Nix Color Sensor ([https://www.nixsensor.com/free-color-](https://www.nixsensor.com/free-color-converter/)
222 [converter/](https://www.nixsensor.com/free-color-converter/)).

223 2.2.3 *Semi-quantification of iron oxide minerals*

224 Diffuse reflectance measurements are extremely useful for the characterization and quantification of
225 solid materials. Indeed, they exhibit attenuation in reflectance spectra due to their light-absorption in
226 specific UV-Vis wavelength ranges. Iron oxide minerals, which are the proper focus of this work,
227 present absorption in association with their electronic transitions within the $3d^5$ shell of Fe^{3+} ion
228 triggered by UV-Vis radiation (Scheinost et al., 1998); as a consequence, reflectance spectra prove
229 as an efficient alternative for their assessment. While past work on PM membranes was mainly based
230 on the first derivative of the UV-Vis reflectance (e.g., Arimoto et al., 2002; Shen et al., 2006), here
231 we compute the second derivative of the Kubelka-Munk (K-M) function spectra. This method has
232 been widely used for the assessment of iron oxides in soil samples (Barrón & Torrent, 1986;
233 Fernandez et al., 1992; Sellitto et al., 2009; Szalai et al., 2013) but less frequently for PM filters
234 analysis (Lafon et al., 2006), while the approach was used in several spectrophotometric applications
235 for the most absorbing aerosol component, i.e. soot (see for example Pandey et al., 2019; Petzold et
236 al., 2004). The calculation of the second derivative was performed using the Savitzky-Golay filter
237 (Schafer, 2011), an averaging algorithm that fits a polynomial to the spectral data allowing the
238 calculation of a derivative of this function. In this work a polynomial order of 4 and a number of
239 smoothing points equal to 251 was chosen. Processed spectra thus obtained revealed neat and
240 significant peaks due to the absorption of iron oxide minerals. The heights of these peaks were
241 utilized for semi-quantitative analysis, following peak definition and baseline subtraction. In our
242 work, iron oxide minerals are determined semi-quantitatively for the absence of a series of standards
243 containing known amounts of iron mineral oxides spread on membranes similar to samples. Indeed
244 several efforts were spent to scope, but owing to the lack of homogeneity of artificial hematite-laden
245 filters, standardization was not reached.

The conversion of the reflectance spectra into K-M spectra was carried out using the UV WinLab
2.85 Software (Perkin Elmer Ltd, United Kingdom), while the calculation of the Savitzky-Golay

second derivative was performed by the software The Unscrambler V10.4 (Camo, Oslo, Norway), and the quantification of peak heights was carried out using the Peak Analyzer tool of the OriginPro 2018 software (Northampton, USA).

246 **2.3 Validation of the methodology**

247 *2.3.1 Validation of UV-Vis DRS results*

248 Sample color (subsection 2.2.2) was numerically defined by means of colorimetric parameters
249 described by CIE, and semi-quantitative information about iron oxide minerals (subsection 2.2.3)
250 were achieved by a suitable mathematical treatment of reflectance spectra. In order to validate our
251 spectrophotometric approach, experimental data obtained were compared with elemental iron
252 concentration data ($\mu\text{g cm}^{-2}$) obtained by Proton Induced X-ray Emission (PIXE) carried out on the
253 same PM_{10} filters using a Tandetron 3 MeV accelerator at LABEC (Laboratorio di tecniche nucleari
254 per l'Ambiente e i Beni Culturali, <https://www.ionbeamcenters.eu/RADIATE-project-partners/inf/n/>)
255 at the INFN Section of Florence (Italy) (Lucarelli et al., 2014; Lucarelli et al., 2018). Since the
256 membranes used in this work are made of quartz instead of the typical PTFE suitable for inorganic
257 elemental analysis, PIXE spectra were adequately processed for the intense interference of silicates
258 in the filter medium (Chiari et al., 2018; and Lucarelli et al., 2011; Calzolari et al., 2006). In brief,
259 PM_{10} samples were irradiated in ambient conditions with a 3.0 MeV proton beam with a 5 nA current
260 for 60 s.

Spearman correlation analysis (Akoglu, 2018) was then performed between the UV-Vis DRS outcomes (color parameters and semi-quantitative data of iron oxide minerals) with elemental iron concentration calculated by PIXE and PM_{10} mass load obtained by gravimetry, both expressed in $\mu\text{g cm}^{-2}$ for dimensional consistency.

261 2.3.2 *Diagnosis and validation of Saharan mineral dust events*

262 2.3.2.1 Diagnosis based on PM filters

263 The ultimate goal of this work is to sort out quickly, but safely the PM filters exposed to Saharan
264 Dust transport events from the others.

265 Therefore, Ward's cluster analysis (Ward, 1963) using squared Euclidean distance was employed for
266 the detection of two sample clusters, respectively a cluster indicating the samples subjected to Saharan
267 dust transport events and another cluster for all the other sample cases. After standardization by
268 autoscaling (van den Berg et al., 2006), the colorimetric parameters of CIELCH model (subsection
269 2.2.2) and the semi-quantitative data of iron oxide minerals (subsection 2.2.3) were used as starting
270 variables. The statistical analysis was carried out by means of the software Statistica V.10 (StatSoft
271 Inc., Tulsa, USA).

272 The two clusters obtained were subsequently compared with PM₁₀ data ($\mu\text{g}/\text{m}^3$) in order to associate
273 or exclude, in a binary way, the occurrence of a Saharan dust incursion.

274 2.3.2.2. Back-trajectory ensembles and residence time analysis

275 A residence time analysis of back-trajectory ensembles (Lin, 2012; Lupu & Maenhaut, 2002; Stohl,
276 1998) was carried out to assess and confirm the diagnosis made by UV-Vis DRS.

277 Ensembles of back-trajectories were calculated using the NOAA Hybrid Single Particle Lagrangian
278 Integrated Trajectory (HYSPLIT_4) model (Rolph et al., 2017; Stein et al., 2015). Meteorological
279 data from the ERA-Interim reanalysis (Dee et al., 2011) was used as input for the trajectory
280 calculations with data interpolated into a 0.5-degree grid, in agreement with the 0.5-degree terrain
281 model available in the Hysplit model, and 27 pressure levels from 1000 to 100 hPa. The ensemble is
282 generated by offsetting the meteorological database by one grid point in the horizontal and 0.01 sigma
283 units in the vertical, resulting in 27 back- trajectories (Draxler, 2003). 96-hour kinematic back-

284 trajectory ensembles were calculated starting 200 m above the sampling site at 00, 06, 12, and 18
285 UTC in the period 8 June – 11 October 2016.

286 The trajectory ensembles were subsequently grouped together on the basis of sampling PM resolution.
287 (weekly). The analysis of residence time was based on the number of trajectory endpoints falling
288 within each sampling period over five broad regions (Africa, America, Europe, Mediterranean Sea,
289 and Atlantic Ocean). Furthermore, two additional specific areas such as Mauritania and the Atlantic
290 Ocean at low altitude (below 800 m) were investigated. Subsequently, the frequency of residence
291 time across each area per single PM filter (Ashbaugh et al., 1985; Orza et al., 2013; Xu et al., 2006)
292 as the ratio between the total counts and the total number of endpoints. All the calculations were
293 performed with scripts purposely elaborated with the R programming language (R Core Team,
294 2019). To further support the diagnosis of African dust events, aerosol optical depth (AOD)
295 Collection C6 (Merged Dark Target/Deep Blue) from the Moderate Resolution Imaging
296 Spectroradiometer (MODIS) onboard the Aqua and Terra satellites were retrieved (NASA EOSDIS,
297 worldview tool at <https://worldview.earthdata.nasa.gov>).

298

299 **3. RESULTS AND DISCUSSION**

300 Results and discussion section is organized as follows:

301 (a) Subsection 3.1 reports the colorimetric parameters and the related digitized colours for the
302 analyzed PM filters, highlighting and discussing their differences.

303 (b) Subsection 3.2 details the semi-quantitative results of iron oxide minerals, and their
304 processing from raw reflectance spectra.

305 (c) Subsection 3.3 presents the correlation between the semi-quantitative data of the iron oxide
306 minerals, the elemental iron obtained by Proton Induced X-ray Emission (PIXE) analysis, and
307 the colorimetric parameters.

308 (d) Subsection 3.4 reveals the PM filters that have been subjected to a Saharan Dust transport
309 event by a multivariate approach validated by residence time analysis.

310 **3.1 Colorimetric data and results**

311 For each portion of the PM filter analyzed, the sample color was obtained by the procedure described
312 in subsection 2.2.2. The colorimetric parameters related to the CIELAB (L^* , a^* , b^*) and CIELCH (L^* ,
313 C_{ab}^* , h_{ab}°) models together with the subsequent color obtained for the blank filter (B) and for the 19
314 PM samples (SN1, ...SN19) are reported in Table 1.

315 The collected PM samples present distinct color shades (from gray to red) as a function of the
316 dominating aerosol source during the respective sampling time interval. In order to examine how
317 these samples differ in color, a graphical representation based on chroma (C_{ab}^*) and hue (h_{ab}°) is
318 reported in Figure 3. Figure 3 (a), shows how the blank filter (B) remarkably differs from all the
319 others (SN1, ...SN19). In fact, the blank filter is characterized by a whitish color due to the absence
320 of particulate material, while a greyish-yellowish-reddish color characterizes all the sampled filters,
321 (see the last column to the right of Table 1). Sampled filters in Figure 3 (b) show a defined trend: the
322 grayest samples (like SN15) present a higher hue value and a lower chroma value than other filters
323 while the most reddish samples (like SN12) show a higher value of chroma and a lower value of hue.
324 Instead, the samples with intermediate values of chroma and hue (like SN7) exhibit a browner
325 coloration than the others. This observation agrees with the CIELCH color definition: a lower hue
326 value corresponds to a color tone more shifted towards red, while a higher chroma value corresponds
327 to a more marked color intensity (compared to the gray color that occurs at chroma values close to
328 zero). This demonstrates how the CIELCH color space adequately describes the colors of the analyzed
329 PM filters due to their high chromaticity. In fact, the higher efficiency of the CIELCH model as
330 compared with the CIELAB one in assessing the differences between the more chromatic colors,
331 since C_{ab}^* and h_{ab}° allow a better identification of the more saturated colors than a and b (Schloss et
332 al., 2018).

333 **3.2 Iron oxide minerals**

334 As previously reported in subsection 2.2.3, the calculation of the second derivative of the Kubelka-
335 Munk function spectra was performed over the UV-Vis DRS spectra. This operation allows to identify
336 attenuated peaks due to light absorption by iron oxide minerals, such as akaganéite, feroxyhyte,
337 ferrihydrite, goethite, hematite, lepidocrocite, maghemite, and schwertmannite (Sherman & Waite,
338 1985; Torrent & Barrón, 2002), whose characteristics are reported in Figure 4.

339 According to Scheinost et al., 1998, only the attenuated peak at around 535 nm is specific for a single
340 mineral (hematite), while the other peaks at 420 nm and 480 nm are shared by several other iron
341 oxides. Therefore, the semi-quantitative nature of the spectral data of iron oxide minerals can be
342 deduced for each portion of the PM filter through an appropriate processing of their UV-Vis
343 reflectance spectra. For sake of brevity, from now on graphical plots present the results for only three
344 characteristic filters, namely SN15, SN7, and SN12 (Figure 5). The selection of the filters is not
345 arbitrary, but is based on their representativeness as described in subsection 3.1.

346 Figure 5 (a) depicts the reflectance UV-Vis spectra obtained from our aerosol samples. The raw
347 spectra present a characteristic baseline due to the scattering of the UV-Vis radiation with limited
348 signal decreases. Samples SN7 and SN12 in particular present two bands at around 480 nm and 535
349 nm characterized by an attenuated reflectance due to the absorption by iron oxides (Gonçalves et al.,
350 2012; Torrent & Barrón, 2002), a spectral feature not observed in the sample SN15. Derivative
351 spectroscopy has been therefore explored in order to: (a) correct for baseline effects in spectra to
352 remove non-chemical effects, (b) enhance spectral detail not appreciable in the raw spectrum, and (c)
353 resolve overlapped bands (Ojeda & Rojas, 2013). The treated spectra finally produced three main
354 peaks at 420, 480 and 535 nm, respectively.

An example is reported in Figure 5 (c). The 420 nm peak was discarded as significantly affected by
an instrumental noise due to the lamp shift from Vis to UV at around 380 nm (see Figure 5 (a)).

Average values and the standard deviations of the peak heights obtained from the signals at 480nm and h_530 nm were calculated for the blank filter (B) and for the 19 samples (SN1, ...SN19) starting from the three analyzed portions for each sample, and were reported in Table 2.

355 3.3 Validation of UV-Vis DRS results

356 The similarity between the sample series of iron oxides semi-quantitative data (h_480nm and
357 h_535nm) and elemental iron (Fe) concentration by PIXE can be observed in Figure 6 (a), showing
358 a comparable trend among all the parameters. Scatter plots in Figure 6 (b) indicate a good correlation
359 between these independent parameters. Table 3 reports the Spearman correlation coefficients between
360 CIELCH parameters, iron oxide minerals semi-quantitative data, elemental iron, and PM₁₀. It is
361 shown that iron (Fe) is highly linearly correlated with PM₁₀ (+0.96), confirming that mineral dust is
362 one of the main components in the analyzed samples. A high positive correlation between peak
363 heights at 480 nm and 535 nm and iron concentration is observed (+0.84 and +0.86 respectively)
364 supporting the association between mineral and elemental components as shown in Figure 6. In
365 particular the band at h_535 nm is found as the most significantly associated to the filter color (+0.85
366 with chroma and -0.83 with hue). This result is extremely interesting because, as previously remarked
367 (see section 3.2), this peak is specific to hematite, while the other peak (h_480nm) is associated with
368 a range of different minerals made of iron oxides, including goethite (which is the most abundant iron
369 oxide in Saharan Dust). An increase in chroma and a decrease in hue leads to a higher degree in the
370 redness of the PM filters (see subsection 3.1), which is exactly the characteristic color of hematite
371 (Rossman, 1996). As such, the semi-quantitative data on iron oxide minerals (especially hematite)
372 are strongly related to PM filter colors (especially the red color), and both parameters are indicative
373 of Saharan dust transport events.

374 **3.4 Diagnosis and validation of Saharan mineral dust events**

375 Figure 7 reports the dendrogram obtained from Ward's clustering analysis applied to the UV-Vis DRS
376 results (CIELCH parameters and iron oxide minerals semi-quantitative data), and where two main
377 clusters are identified. In particular, 15 PM samples belong to cluster 1, while the other 4 PM samples
378 belong to cluster 2. These clusters are compared with PM₁₀ data (normalized in air sampled volume,
379 $\mu\text{g}/\text{m}^3$) in Figure 8 (a). Indeed, the association of mineral dust transport events has already been
380 clearly related to significant increases in PM due to the considerable mass load of this component in
381 particulate material owing to the large fraction of the coarse particles (Krasnov et al., 2014; Matassoni
382 et al., 2011). In order to facilitate the Saharan Dust detection, the UV-Vis DRS results are reported
383 again in Figure 8(b) and Figure 8(c). The residence time spent by the air parcels over different areas
384 before reaching the sampling site is also reported in Figure 9 for each PM sample.

385 Cluster 1 (highlighted in red) clearly identifies the Saharan dust events while cluster 2 (highlighted
386 in green) identifies air masses from all the other source areas (Figure 8(a)). Moreover, these results
387 are in agreement with the estimated residence time (Figure 9 (a)). Indeed, residence time analysis
388 highlights how SN2, SN15, and SN19 samples belonging to cluster 2 are characterized by shorter
389 residence times (less than 10%) over Africa than other PM filters (higher than 10%), suggesting uplift
390 and rapid transport of mineral dust from the North-African desert without appreciable mixing with
391 other aerosol sources.

392 Sample SN1 presents an exception being characterized by an elevated PM₁₀ value and a residence
393 time over Africa comparable to the samples belonging to the Saharan dust events cluster (cluster 1).
394 Its assignment to the category of non-Saharan dust events, obtained only by UV-Vis DRS, is linked
395 to its greyish color and to the low concentrations of iron oxide minerals. In order to justify this
396 outcome, an in-depth analysis was carried out by satellite images retrieved from NASA's Earth
397 Observing System Data and Information System (EOSDIS) (Behnke et al., 2019), reported in Figure

398 10. Whitish dust from the dried surface of Chott el-Jerid ephemeral lake (Figure 10(a)), was uplifted
399 by the wind on 05/06/2016 (Figure 10(b)) and reached the receptor site on 08/06/2016 (from Figure
400 10(c) to Figure 10(f)), that is the first day of SN1 filter sampling period. Therefore, although the SN1
401 sample is significantly impacted by this Saharan dust transport event, its chemical-mineralogical
402 composition is unusual compared to other PM samples due to the deficiency of iron oxide minerals,
403 as evidenced by the grayish color of the examined filter.

404 Some particular considerations can be drawn also for two additional specific samples; i.e. SN12 and
405 SN19. SN12 is one of the PM filters more impacted by a Saharan dust events, as results from its high
406 PM₁₀ concentration and the pronounced reddish color, (see subsection 3.1). The latter observation
407 may be explained by the higher value of residence time over Mauritania (> 4%), as reported in Figure
408 9 (b), whose area is known to be an important source of hematite (Journet et al., 2014; Schlueter,
409 2006; Waele et al., 2019). As previously assessed, sample SN19 is clearly a PM sample not affected
410 by Saharan dust transport. This filter presents the “whitest” color amongst the samples analysed, as
411 shown by the highest luminescence value ($L^* = 73.23$, look at Table 1) in the CIELAB/CIELCH
412 colorimetric models. This result can be justified by a significantly long residence time over the
413 Atlantic Ocean at low altitude (> 5%), as reported in Figure 9 (c), which presumably involves a strong
414 influence of colorless sea salt component (mainly defined by sodium chloride and magnesium
415 chloride) in the examined filter.

416

417 **4. CONCLUSIONS**

418 In this work, the feasibility of UV-Vis Diffuse Reflectance Spectroscopy for a rapid and non-
419 destructive diagnosis of Saharan dust events in particulate matter filters has been explored, assessed,
420 and validated. This method has been applied to a sequence of particulate matter filters sampled at

421 high altitude (2550 m a.s.l.) in an area heavily impacted by Saharan mineral dust incursion events due
422 to its proximity to North Africa (Sierra Nevada, Spain, 37.096 N, -3.387 W).

423 In particular, this analytical method allowed to identify unequivocally two absorption bands
424 corresponding to a well-defined set of iron mineral oxides contained in Saharan dust: the absorption
425 band at about 480 nm, representative of multiple iron oxide minerals (i.e., goethite, lepidocrocite,
426 maghemite, ferrihydrite, ferrosulphate, akaganéite, and schwertmannite), and another at about 535 nm,
427 specific for hematite and therefore highly selective for diagnostic purposes. Through appropriate
428 processing of the reflectance spectra, a semi-quantitative data for these mineral oxides it was
429 obtained. Furthermore, starting from the reflectance measurements, it was possible to quantitatively
430 parameterize the filter coloring as a function of PM source.

431 The results obtained from this technique have been validated on the basis of the elemental iron
432 concentration obtained by Proton Induced X-ray Emission (PIXE) analysis. Besides, the relationship
433 between the concentration of hematite increases and the higher reddish color of the filters with an
434 increase in their PM₁₀ content was demonstrated. Therefore, the UV-Vis DRS has been proven to be
435 extremely useful for a fast, cheap, and unambiguous identification of Saharan mineral dust events in
436 PM filters.

437 The results obtained have been finally proven on the basis of residence time analysis of back-
438 trajectory ensembles, whose outcomes are in excellent agreement with those obtained by UV-Vis
439 DRS, except for one PM sample with a peculiar chemical-mineralogical composition likely associated
440 with the dried Chott el-Jerid Lake (Tunisia). Furthermore, some other samples have been explored
441 by associating the color and the semi-quantitative data of iron oxide minerals with their particular PM
442 sources.

443 It is important to highlight that in this work the UV-Vis DRS methodology was described, applied,
444 and validated for weekly PM₁₀ samples certainly characterized by a predominance of Saharan Dust

445 but likewise affected by a complex mixture of emission sources. Despite the presence of high number
446 of mixed emission sources, reasonable outcomes were achieved with this technique. The final
447 decision in using this approach is currently under investigation for other daily PM filters presenting
448 significant amounts of anthropogenic particulate matter, e.g. Black and Brown carbon, which can
449 significantly affect the sample membranes' spectral behavior.

450

451 **ACKNOWLEDGEMENTS**

452 This work has been carried out under the Spanish project FRESA (Impact of dust-laden African air
453 masses and of stratospheric air masses in the Iberian Peninsula. Role of the Atlas Mountains, Ref:
454 CGL2015-70741-R). Firstly, Lucas Alados-Arboledas (IISTA-CEAMA) is gratefully acknowledged
455 for making possible the field campaign at the sampling site. A Heartfelt thanks to Christian Cingolani,
456 Josep Mestres Sanna, and Adrià Simon Ortiz for the assistance in the experimental activity during
457 their thesis work. Finally, the authors acknowledge the NOAA Air Resources Laboratory (ARL) for
458 the provision of the HYSPLIT transport and dispersion model and/or READY website
459 (<https://www.ready.noaa.gov>) used in this publication and the European Centre for Medium-range
460 Weather Forecast (ECMWF) for making available the ERA-Interim database.

461

462 **REFERENCES**

463 Akoglu, H. (2018). User's guide to correlation coefficients. Turkish Journal of Emergency Medicine,
464 18. <https://doi.org/10.1016/j.tjem.2018.08.001>

465 Alastuey, A., Querol, X., Aas, W., Lucarelli, F., Pérez, N., Moreno, T., ... Yttri, K. E. (2016).
466 Geochemistry of PM10 over Europe during the EMEP intensive measurement periods in summer

467 2012 and winter 2013. *Atmos. Chem. Phys.*, 16(10), 6107–6129. <https://doi.org/10.5194/acp-16->
468 6107-2016

469 Alfaro, S., Lafon, S., Rajot, J., Formenti, P., Gaudichet, A., & Maillé, M. (2004). Iron oxides and
470 light absorption by pure desert dust: An experimental study. *Journal of Geophysical Research*
471 (Atmospheres), 109, 8208. <https://doi.org/10.1029/2003JD004374>

472 Arimoto, R., Balsam, W., & Schloesslin, C. (2002). Visible spectroscopy of aerosol particles
473 collected on filters: Iron-oxide minerals. *Atmospheric Environment*, 36, 89–96.
474 [https://doi.org/10.1016/S1352-2310\(01\)00465-4](https://doi.org/10.1016/S1352-2310(01)00465-4)

475 Ashbaugh, L. L., Malm, W. C., & Sadeh, W. Z. (1985). A residence time probability analysis of sulfur
476 concentrations at grand Canyon National Park. *Atmospheric Environment* (1967), 19(8), 1263–1270.
477 [https://doi.org/https://doi.org/10.1016/0004-6981\(85\)90256-2](https://doi.org/https://doi.org/10.1016/0004-6981(85)90256-2)

478 Barnaba, F., Bolignano, A., di Liberto, L., Morelli, M., Lucarelli, F., Nava, S., ... Gobbi, G. P. (2017).
479 Desert dust contribution to PM10 loads in Italy: Methods and recommendations addressing the
480 relevant European Commission Guidelines in support to the Air Quality Directive 2008/50.
481 *Atmospheric Environment*, 161. <https://doi.org/10.1016/j.atmosenv.2017.04.038>

482 Barrón, V., & Torrent, J. (1986). Use of the Kubelka—Munk theory to study the influence of iron
483 oxides on soil colour. *Journal of Soil Science*, 37(4), 499–510.

484 Behnke, J., Mitchell, A., & Ramapriyan, H. (2019). NASA's Earth Observing Data and Information
485 System – Near-Term Challenges. *Data Science Journal*, 18. <https://doi.org/10.5334/dsj-2019-040>

486 Blitz, J. P. (1998). Diffuse reflectance spectroscopy. *Modern Techniques in Applied Molecular*
487 *Spectroscopy*, 14, 185.

488 Bonasoni, P., Cristofanelli, P., Sandro, F., Gobbi, G. P., van Dingenen, R., Tositti, L., & Balkanski,
489 Y. (2003). Ozone and aerosol correlation during Saharan dust transport episodes at Mt. Cimone.

490 Brattich, E, Hernández-Ceballos, M. A., Cinelli, G., & Tositti, L. (2015a). Analysis of ²¹⁰Pb peak
491 values at Mt. Cimone (1998–2011). *Atmospheric Environment*, 112, 136–147.
492 <https://doi.org/https://doi.org/10.1016/j.atmosenv.2015.04.020>

493 Brattich, Erika, Riccio, A., Tositti, L., Cristofanelli, P., & Bonasoni, P. (2015b). An outstanding
494 Saharan dust event at Mt. Cimone (2165 m asl, Italy) in March 2004. *Atmospheric Environment*, 113,
495 223–235.

496 Bristow, C. S., Hudson-Edwards, K. A., & Chappell, A. (2010). Fertilizing the Amazon and equatorial
497 Atlantic with West African dust. *Geophysical Research Letters*, 37(14).

498 Cabello, M., G. Orza, J., Dueñas, C., Liger, E., Gordo, E., & Cañete, S. (2016). Back-trajectory
499 analysis of African dust outbreaks at a coastal city in southern Spain: Selection of starting heights
500 and assessment of African and concurrent Mediterranean contributions. *Atmospheric Environment*,
501 140. <https://doi.org/10.1016/j.atmosenv.2016.05.047>

502 Calzolari, G., Chiari, M., García Orellana, I., Lucarelli, F., Migliori, A., Nava, S., & Taccetti, F.
503 (2006). The new external beam facility for environmental studies at the Tandatron accelerator of
504 LABEC. *Nuclear Instruments and Methods in Physics Research Section B: Beam Interactions with*
505 *Materials and Atoms*, 249(1), 928–931. <https://doi.org/https://doi.org/10.1016/j.nimb.2006.03.193>

506 Caquineau, S., Gaudichet, A., Gomes, L., & Legrand, M. (2002). Mineralogy of Saharan dust
507 transported over northwestern tropical Atlantic Ocean in relation to source regions. *Journal of*
508 *Geophysical Research: Atmospheres*, 107(D15), AAC 4-1-AAC 4-12.
509 <https://doi.org/10.1029/2000JD000247>

510 Chiari, M., Yubero, E., Calzolari, G., Lucarelli, F., Crespo, J., Galindo, N., ... Nava, S. (2018).
511 Comparison of PIXE and XRF analysis of airborne particulate matter samples collected on Teflon
512 and quartz fibre filters. *Nuclear Instruments and Methods in Physics Research Section B: Beam*

513 Interactions with Materials and Atoms, 417, 128–132.
514 <https://doi.org/https://doi.org/10.1016/j.nimb.2017.07.031>

515 Chin, M., Diehl, T., Dubovik, O., Eck, T., Holben, B., Sinyuk, A., & Streets, D. (2009). Light
516 absorption by pollution, dust, and biomass burning aerosols: A global model study and evaluation
517 with AERONET measurements. *Annales Geophysicae*, 27. [https://doi.org/10.5194/angeo-27-3439-](https://doi.org/10.5194/angeo-27-3439-2009)
518 2009

519 Cuevas, E., Gómez-Peláez, A. J., Rodríguez, S., Terradellas, E., Basart, S., García, R. D., ... Alonso-
520 Pérez, S. (2017). The pulsating nature of large-scale Saharan dust transport as a result of interplays
521 between mid-latitude Rossby waves and the North African Dipole Intensity. *Atmospheric*
522 *Environment*, 167, 586–602.

523 Cusack, M., Alastuey, A., Pérez, N., Pey, J., & Querol, X. (2012). Trends of particulate matter (PM_{2.5})
524 and chemical composition at a regional background site in the Western Mediterranean over the last
525 nine years (2002–2010). *Atmos. Chem. Phys.*, 12(18), 8341–8357.

526 Dee, D., P, de, Uppala, Simmons, Berrisford, Poli, P., ... Vitart, F. (2011). The ERA-Interim
527 reanalysis: Configuration and performance of the data assimilation system. *Quarterly Journal of the*
528 *Royal Meteorological Society*, 137, 553–597. <https://doi.org/10.1002/qj.828>

529 Diapouli, E., Manousakas, M. I., Vratolis, S., Vasilatou, V., Pateraki, S., Bairachtari, K. A., ...
530 Eleftheriadis, K. (2017). AIRUSE-LIFE +: estimation of natural source contributions to urban
531 ambient air PM₁₀ and PM_{2.5} concentrations in southern Europe – implications to compliance with
532 limit values. *Atmos. Chem. Phys.*, 17(5), 3673–3685. <https://doi.org/10.5194/acp-17-3673-2017>

533 Dickerson, R., Kondragunta, S., Stenchikov, G., Civerolo, K., Doddridge, B., & Holben, B. (1997).
534 The impact of aerosol on solar UV radiation and photochemical smog. *Science (New York, N.Y.)*,
535 278, 827–830. <https://doi.org/10.1126/science.278.5339.827>

536 Draxler, R. R. (2003). Evaluation of an Ensemble Dispersion Calculation. *Journal of Applied*
537 *Meteorology*, 42(2), 308–317. [https://doi.org/10.1175/1520-](https://doi.org/10.1175/1520-0450(2003)042<0308:EOAEDC>2.0.CO;2)
538 [0450\(2003\)042<0308:EOAEDC>2.0.CO;2](https://doi.org/10.1175/1520-0450(2003)042<0308:EOAEDC>2.0.CO;2)

539 EC Commission (2011). Staff Working Paper establishing guidelines for determination of
540 contributions from the re-suspension of particulates following winter sanding or salting of roads under
541 the Directive 2008/50/EC on ambient air quality and cleaner air for Europe. European Commission,
542 SEC. 2011; 2011:207.
543 http://ec.europa.eu/environment/air/quality/legislation/pdf/sec_2011_0207.pdf

544 EEA, Technical report No 10/2012 (2012). Particulate matter from natural sources and related
545 reporting under the EU Air Quality Directive in 2008 and 2009. ISBN: 978-92-9213-325-2.
546 <https://www.eea.europa.eu/publications/particulate-matter-from-natural-sources>

547 Escudero, M., Castillo, S., Querol, X., Avila, A., Alarcón, M., Viana, M. M., ... Rodríguez, S. (2005).
548 Wet and dry African dust episodes over eastern Spain. *Journal of Geophysical Research:*
549 *Atmospheres*, 110(D18). <https://doi.org/10.1029/2004JD004731>

550 Escudero, M., Querol, X., Pey, J., Alastuey, A., Pérez, N., Ferreira, F., ... Cuevas, E. (2007). A
551 methodology for the quantification of the net African dust load in air quality monitoring networks.
552 *Atmospheric Environment*, 41(26), 5516–5524.
553 <https://doi.org/https://doi.org/10.1016/j.atmosenv.2007.04.047>

554 EU (2008). Directive 2008/50/EC of the European Parliament and of the Council of 21 May 2008 on
555 ambient air quality and cleaner air for Europe. Official Journal of the European Union.

556 Fernandez, R. N., & Schulze, D. G. (1992). Munsell colors of soils simulated by mixtures of goethite
557 and hematite with kaolinite. *Zeitschrift Für Pflanzenernährung Und Bodenkunde*, 155(5), 473–478.

558 Flentje, H., Briel, B., Beck, C., Collaud Coen, M., Fricke, M., Cyrus, J., ... Thomas, W. (2015).
559 Identification and monitoring of Saharan dust: An inventory representative for south Germany since
560 1997. *Atmospheric Environment*, 109, 87–96.
561 <https://doi.org/https://doi.org/10.1016/j.atmosenv.2015.02.023>

562 Formenti, P., Caquineau, S., Chevallier, S., Klaver, A., Desboeufs, K., Rajot, J., ... Briois, V. (2014).
563 Dominance of goethite over hematite in iron oxides of mineral dust from Western Africa: quantitative
564 partitioning by X-ray Absorption Spectroscopy. *Journal of Geophysical Research: Atmospheres*, 119.
565 <https://doi.org/10.1002/2014JD021668>

566 Formenti, P., Nava, S., Prati, P., Chevallier, S., Klaver, A., Lafon, S., ... Chiari, M. (2010). Self-
567 attenuation artifacts and correction factors of light element measurements by X-ray analysis:
568 Implication for mineral dust composition studies. *Journal of Geophysical Research*, 115.
569 <https://doi.org/10.1029/2009JD012701>

570 Formenti, P., Rajot, J., Desboeufs, K., Caquineau, S., Chevallier, S., Nava, S., ... Highwood, E.
571 (2008). Regional variability of the composition of mineral dust from western Africa: Results from
572 the AMMA SOP0/DABEX and DODO field campaigns. *J. Geophys. Res.*, 113.
573 <https://doi.org/10.1029/2008JD009903>

574 Garrison, V. H., Shinn, E. A., Foreman, W. T., Griffin, D. W., Holmes, C. W., Kellogg, C. A., ...
575 Smith, G. W. (2003). African and Asian Dust: From Desert Soils to Coral Reefs. *BioScience*, 53(5),
576 469–480. [https://doi.org/10.1641/0006-3568\(2003\)053\[0469:AAADFD\]2.0.CO;2](https://doi.org/10.1641/0006-3568(2003)053[0469:AAADFD]2.0.CO;2)

577 Ginoux, P. (2017). Warming or cooling dust? *Nature Geoscience*, 10(4), 246–248.
578 <https://doi.org/10.1038/ngeo2923>

579 Gonçalves, Í. G., Petter, C. O., & Machado, J. L. (2012). Quantification of hematite and goethite
580 concentrations in kaolin using diffuse reflectance spectroscopy: a new approach to Kubelka-Munk
581 theory. *Clays and Clay Minerals*, 60(5), 473–483.

582 Goudie, A., & Middleton, N. (2006). Desert Dust in the Global System. *Desert Dust in the Global*
583 *System*, 1–287. <https://doi.org/10.1007/3-540-32355-4>

584 Ibraheem, N., Hasan, M., Khan, R. Z., & Mishra, P. (2012). Understanding Color Models: A Review.
585 *ARNP Journal of Science and Technology*, 2.

586 IDSO, S. (1981). Climatic change: The role of atmospheric dust. *Special Paper of the Geological*
587 *Society of America*, 186, 207–215. <https://doi.org/10.1130/SPE186-p207>

588 ISO-CIE 11664-1-2019. Colorimetry - CIE standard colorimetric observers. Standard, International
589 Organization for Standardization, Geneva, CH.

590 ISO-CIE 11664-2-2020. Colorimetry - Part 2: CIE standard illuminants. Standard, International
591 Organization for Standardization, Geneva, CH.

592 ISO-CIE 11664-4-2019. Colorimetry - Part 4: CIE 1976 L*a*b* colour space. Standard, International
593 Organization for Standardization, Geneva, CH.

594 Israelevich, P., Ganor, E., Alpert, P., Kishcha, P., & Stupp, A. (2012). Predominant transport paths
595 of Saharan dust over the Mediterranean Sea to Europe. *Journal of Geophysical Research:*
596 *Atmospheres*, 117(D2).

597 Journet, E., Balkanski, Y., & Harrison, S. (2014). A new data set of soil mineralogy for dust-cycle
598 modeling. *ATMOSPHERIC CHEMISTRY AND PHYSICS*, 14, 3801–3816.
599 <https://doi.org/10.5194/acp-14-3801-2014>

600 Karanasiou, A., Moreno, N., Moreno, T., Viana, M., de Leeuw, F., & Querol, X. (2012). Health
601 effects from Sahara dust episodes in Europe: Literature review and research gaps. *Environment*
602 *International*, 47, 107–114. <https://doi.org/10.1016/j.envint.2012.06.012>

603 Krasnov, H., Katra, I., Koutrakis, P., & Friger, M. (2014). Contribution of dust storms to PM10 levels
604 in an urban arid environment. *Journal of the Air & Waste Management Association* (1995), 64, 89–
605 94. <https://doi.org/10.1080/10962247.2013.841599>

606 Kremers, J., Baraas, R., & Marshall, N. (2016). Human Color Vision. [https://doi.org/10.1007/978-3-](https://doi.org/10.1007/978-3-319-44978-4)
607 319-44978-4

608 Lafon, S., Sokolik, I., Rajot, J., Caquineau, S., & Gaudichet, A. (2006). Characterization of iron
609 oxides in mineral dust aerosols: Implications for light absorption. *Journal of Geophysical Research*,
610 111. <https://doi.org/10.1029/2005JD007016>

611 Lin, J. (2012). Lagrangian Modeling of the Atmosphere: An Introduction. In *Geophysical Monograph*
612 *Series* (Vol. 200). <https://doi.org/10.1029/2012GM001376>

613 Linke, C., Möhler, O., Veres, A., Mohácsi, Á., Bozóki, Z., Szabó, G., & Schnaiter, M. (2006). Optical
614 properties and mineralogical composition of different Saharan mineral dust samples: a laboratory
615 study. *Atmos. Chem. Phys.*, 6(11), 3315–3323. <https://doi.org/10.5194/acp-6-3315-2006>

616 Littmann, T., & Steinrücke, J. (1989). Atmospheric boundary conditions of recent Saharan dust influx
617 into Central Europe. *GeoJournal*, 18, 399–406. <https://doi.org/10.1007/BF00772694>

618 Lucarelli, F., Calzolari, G., Chiari, M., Giannoni, M., Mochi, D., Nava, S., & Carraresi, L. (2014). The
619 upgraded external-beam PIXE/PIGE set-up at LABEC for very fast measurements on aerosol
620 samples. *Nuclear Instruments and Methods in Physics Research Section B: Beam Interactions with*
621 *Materials and Atoms*, 318, 55–59. <https://doi.org/https://doi.org/10.1016/j.nimb.2013.05.099>

622 Lucarelli, F., Calzolari, G., Chiari, M., Nava, S., & Carraresi, L. (2018). Study of atmospheric aerosols
623 by IBA techniques: The LABEC experience. *Nuclear Instruments and Methods in Physics Research*
624 *Section B: Beam Interactions with Materials and Atoms*, 417, 121–127.
625 <https://doi.org/https://doi.org/10.1016/j.nimb.2017.07.034>

626 Lucarelli, F., Nava, S., Calzolari, G., Chiari, M., Udisti, R., & Marino, F. (2011). Is PIXE still a useful
627 technique for the analysis of atmospheric aerosols? The LABEC experience. *X-Ray Spectrometry*,
628 40, 162–167. <https://doi.org/10.1002/xrs.1312>

629 Lupu, A., & Maenhaut, W. (2002). Application and comparison of two statistical trajectory
630 techniques for identification of source regions of atmospheric aerosol species. *Atmospheric*
631 *Environment*, 36(36), 5607–5618. [https://doi.org/https://doi.org/10.1016/S1352-2310\(02\)00697-0](https://doi.org/https://doi.org/10.1016/S1352-2310(02)00697-0)

632 Marconi, M., Sferlazzo, D. M., Becagli, S., Bommarito, C., Calzolari, G., Chiari, M., ... Udisti, R.
633 (2014). Saharan dust aerosol over the central Mediterranean Sea: PM10 chemical composition and
634 concentration versus optical columnar measurements. *Atmos. Chem. Phys.*, 14(4), 2039–2054.
635 <https://doi.org/10.5194/acp-14-2039-2014>

636 Matassoni, L., Pratesi, G., Centioli, D., Cadoni, F., Lucarelli, F., Nava, S., & Malesani, P. (2011).
637 Saharan dust contribution to PM 10, PM 2.5 and PM 1 in urban and suburban areas of Rome: A
638 comparison between single-particle SEM-EDS analysis and whole-sample PIXE analysis. *Journal of*
639 *Environmental Monitoring : JEM*, 13, 732–742. <https://doi.org/10.1039/c0em00535e>

640 Menéndez, I., Díaz-Hernández, J. L., Mangas, J., Alonso, I., & Sánchez-Soto, P. J. (2007). Airborne
641 dust accumulation and soil development in the North-East sector of Gran Canaria (Canary Islands,
642 Spain). *Journal of Arid Environments*, 71(1), 57–81.
643 <https://doi.org/https://doi.org/10.1016/j.jaridenv.2007.03.011>

644 Middleton, N., & Goudie, A. (2002). Saharan dust: Sources and trajectories. *Transactions of the*
645 *Institute of British Geographers*, 26, 165–181. <https://doi.org/10.1111/1475-5661.00013>

646 Molinaroli, E., & Masiol, M. (2006). Particolato atmosferico e ambiente mediterraneo. Il caso delle
647 polveri sahariane.

648 Nava, S., Becagli, S., Calzolari, G., Chiari, M., Lucarelli, F., Prati, P., ... Vecchi, R. (2012). Saharan
649 dust impact in central Italy: An overview on three years elemental data records. *Atmospheric*
650 *Environment*, 60, 444–452. <https://doi.org/https://doi.org/10.1016/j.atmosenv.2012.06.064>

651 WHO (2006). WHO Air quality guidelines for particulate matter, ozone, nitrogen dioxide and sulfur
652 dioxide: global update 2005: summary of risk assessment (p. WHO/SDE/PHE/OEH/06.02). p.
653 WHO/SDE/PHE/OEH/06.02. World Health Organization.

654 Ojeda, C. B., & Rojas, F. S. (2013). Recent applications in derivative ultraviolet/visible absorption
655 spectrophotometry: 2009–2011: a review. *Microchemical Journal*, 106, 1–16.

656 Orza, J. A. G., Cabello, M., Galiano, V., Vermeulen, A. T., & Stein, A. F. (2013). The Association
657 Between the North Atlantic Oscillation and the Interannual Variability of the Tropospheric Transport
658 Pathways in Western Europe. In *Lagrangian Modeling of the Atmosphere* (pp. 127–142).
659 <https://doi.org/10.1029/2012GM001315>

660 Pandey, A., Shetty, N. J., & Chakrabarty, R. K. (2019). Aerosol light absorption from optical
661 measurements of PTFE membrane filter samples: sensitivity analysis of optical depth measures.
662 *Atmos. Meas. Tech.*, 12(2), 1365–1373. <https://doi.org/10.5194/amt-12-1365-2019>

663 Pérez, C., Haustein, K., Janjic, Z., Jorba, O., Huneus, N., Baldasano, J. M., Black, T., Basart, S.,
664 Nickovic, S., Miller, R. L., Perlwitz, J. P., Schulz, M., & Thomson, M. (2011). Atmospheric dust
665 modeling from meso to global scales with the online NMMB/BSC-Dust model – Part 1: Model

666 description, annual simulations and evaluation. *Atmos. Chem. Phys.*, 11(24), 13001–13027.
667 <https://doi.org/10.5194/acp-11-13001-2011>

668 Petzold, A., & Schönlinner, M. (2004). Multi-angle absorption photometry—a new method for the
669 measurement of aerosol light absorption and atmospheric black carbon. *Journal of Aerosol Science*,
670 35(4), 421–441. <https://doi.org/https://doi.org/10.1016/j.jaerosci.2003.09.005>

671 Prospero, J., Schmitt, R., Cuevas, E., Savoie, D., Graustein, W., Turekian, K., ... II, H. (1995).
672 Temporal variability of summer-time ozone and aerosols in the free troposphere over the eastern
673 North Atlantic. *Geophysical Research Letters*, 22, 2925–2928. <https://doi.org/10.1029/95GL02791>

674 Putaud, J.-P., van Dingenen, R., Dell’Acqua, A., Raes, F., Matta, E., Decesari, S., ... Fuzzi, S. (2004).
675 Size-segregated aerosol mass closure and chemical composition in Monte Cimone (I) during
676 MINATROC.

677 Querol, X., Tobías, A., Pérez, N., Karanasiou, A., Amato, F., Stafoggia, M., ... Alastuey, A. (2019).
678 Monitoring the impact of desert dust outbreaks for air quality for health studies. *Environment*
679 *International*, 130, 104867. <https://doi.org/https://doi.org/10.1016/j.envint.2019.05.061>

680 R Core Team (2019). *R: A language and environment for statistical computing*. R Foundation for
681 Statistical Computing, Vienna, Austria. URL <https://www.R-project.org/>.

682 Reicher, N., Budke, C., Eickhoff, L., Raveh-Rubin, S., Kaplan-Ashiri, I., Koop, T., & Rudich, Y.
683 (2019). Size-dependent ice nucleation by airborne particles during dust events in the eastern
684 Mediterranean. *Atmos. Chem. Phys.*, 19(17), 11143–11158. [https://doi.org/10.5194/acp-19-11143-](https://doi.org/10.5194/acp-19-11143-2019)
685 2019

686 Remoundaki, E., Bourliva, A., Kokkalis, P., Mamouri, R. E., Papayannis, A., Grigoratos, T., ...
687 Tsezos, M. (2011). PM10 composition during an intense Saharan dust transport event over Athens

688 (Greece). *Science of The Total Environment*, 409(20), 4361–4372.
689 <https://doi.org/https://doi.org/10.1016/j.scitotenv.2011.06.026>

690 Riccio, A., Chianese, E., Tositti, L., Baldacci, D., & Sandrini, S. (2009). Modeling the transport of
691 Saharan dust toward the Mediterranean region: an important issue for its ecological implications.
692 *Ecological Questions*, 11, 65–72.

693 Rodríguez, S., Calzolari, G., Chiari, M., Nava, S., García, M. I., López-Solano, J., ... Querol, X.
694 (2020). Rapid changes of dust geochemistry in the Saharan Air Layer linked to sources and
695 meteorology. *Atmospheric Environment*, 223, 117186.
696 <https://doi.org/https://doi.org/10.1016/j.atmosenv.2019.117186>

697 Rolph, G., Stein, A., & Stunder, B. (2017). Real-time Environmental Applications and Display
698 sYstem: READY. *Environmental Modelling & Software*, 95, 210–228.
699 <https://doi.org/https://doi.org/10.1016/j.envsoft.2017.06.025>

700 Rossman, G. (1996). Why hematite is red: Correlation of optical absorption intensities and magnetic
701 moments of Fe³⁺ minerals. 5, 23–27.

702 Schafer, R. (2011). What Is a Savitzky-Golay Filter? [Lecture Notes]. *IEEE Signal Processing*
703 *Magazine* - *IEEE SIGNAL PROCESS MAG*, 28, 111–117.
704 <https://doi.org/10.1109/MSP.2011.941097>

705 Scheinost, A., Chavernas, A., Barrón, V., & Torrent, J. (1998). Use and limitations of second-
706 derivative diffuse reflectance spectroscopy in the visible to near-infrared range to identify and
707 quantify Fe oxides in soils. *Clays and Clay Minerals*, 46, 528–536.
708 <https://doi.org/10.1346/CCMN.1998.0460506>

709 Schloss, K. B., Lessard, L., Racey, C., & Hurlbert, A. C. (2018). Modeling color preference using
710 color space metrics. *Vision Research*, 151, 99–116.
711 <https://doi.org/https://doi.org/10.1016/j.visres.2017.07.001>

712 Schlueter, T. (2006). Geological Atlas of Africa: With Notes on Stratigraphy, Tectonics, Economic
713 Geology, Geohazards and Geosites of Each Country. <https://doi.org/10.1007/3-540-29145-8>

714 Sellitto, V., Barrón, V., Palumbo, G., Salzano, R., & Colombo, C. (2008). Uso della spettrometria di
715 riflettanza diffusa (DRS) e bi-direzionale (BRF) per lo studio dei suoli vulcanici europei.

716 Sellitto, V. M., Fernandes, R. B. A., Barrón, V., & Colombo, C. (2009). Comparing two different
717 spectroscopic techniques for the characterization of soil iron oxides: Diffuse versus bi-directional
718 reflectance. *Geoderma*, 149(1–2), 2–9.

719 Shao, L., Li, W., Yang, S., Shi, Z., & Lü, S. (2007). Mineralogical characteristics of airborne particles
720 collected in Beijing during a severe Asian dust storm period in spring 2002. *Science in China Series*
721 *D: Earth Sciences*, 50(6), 953–959. <https://doi.org/10.1007/s11430-007-0035-7>

722 Shen, Z. X., Cao, J. J., Zhang, X. Y., Arimoto, R., Ji, J. F., Balsam, W. L., ... Li, X. X. (2006).
723 Spectroscopic analysis of iron-oxide minerals in aerosol particles from northern China. *Science of*
724 *the Total Environment*, 367(2–3), 899–907.

725 Sherman, D. M., & Waite, T. D. (1985). Electronic spectra of Fe³⁺ oxides and oxide hydroxides in
726 the near IR to near UV. *American Mineralogist*, 70(11–12), 1262–1269. Retrieved from
727 <http://pubs.er.usgs.gov/publication/70012311>

728 Shi, Z., Krom, M. D., Jickells, T. D., Bonneville, S., Carslaw, K. S., Mihalopoulos, N., ... Benning,
729 L. G. (2012). Impacts on iron solubility in the mineral dust by processes in the source region and the
730 atmosphere: A review. *Aeolian Research*, 5, 21–42.
731 <https://doi.org/https://doi.org/10.1016/j.aeolia.2012.03.001>

732 Shinn, E. A., Smith, G. W., Prospero, J. M., Betzer, P., Hayes, M. L., Garrison, V., & Barber, R. T.
733 (2000). African dust and the demise of Caribbean Coral Reefs. *Geophysical Research Letters*, 27(19),
734 3029–3032. <https://doi.org/10.1029/2000GL011599>

735 Sokolik, I. N., & Toon, O. B. (1999). Incorporation of mineralogical composition into models of the
736 radiative properties of mineral aerosol from UV to IR wavelengths. *Journal of Geophysical Research:*
737 *Atmospheres*, 104(D8), 9423–9444. <https://doi.org/10.1029/1998JD200048>

738 Soleimani, Z., Teymouri, P., Darvishi Bolorani, A., Mesdaghinia, A., Middleton, N., & Griffin, D.
739 W. (2020). An overview of bioaerosol load and health impacts associated with dust storms: A focus
740 on the Middle East. *Atmospheric Environment*, 223, 117187.
741 <https://doi.org/https://doi.org/10.1016/j.atmosenv.2019.117187>

742 Spyrou, C., Mitsakou, C., Kallos, G., Louka, P., & Vlastou, G. (2010). An improved limited area
743 model for describing the dust cycle in the atmosphere. *Journal of Geophysical Research:*
744 *Atmospheres*, 115(D17). <https://doi.org/https://doi.org/10.1029/2009JD013682>

745 Stafoggia, M., Zauli-Sajani, S., Pey, J., Samoli, E., Alessandrini, E., Basagaña, X., ... Díaz, J. (2016).
746 Desert dust outbreaks in Southern Europe: contribution to daily PM10 concentrations and short-term
747 associations with mortality and hospital admissions. *Environmental Health Perspectives*, 124(4),
748 413–419.

749 Stein, A. F., Draxler, R. R., Rolph, G. D., Stunder, B. J. B., Cohen, M. D., & Ngan, F. (2015).
750 NOAA's HYSPLIT Atmospheric Transport and Dispersion Modeling System. *Bulletin of the*
751 *American Meteorological Society*, 96(12), 2059–2077. <https://doi.org/10.1175/BAMS-D-14-00110.1>

752 Stohl, A. (1998). Computation, accuracy and applications of trajectories—A review and bibliography.
753 *Atmospheric Environment*, 32(6), 947–966. [https://doi.org/https://doi.org/10.1016/S1352-](https://doi.org/https://doi.org/10.1016/S1352-2310(97)00457-3)
754 [2310\(97\)00457-3](https://doi.org/https://doi.org/10.1016/S1352-2310(97)00457-3)

755 Szalai, Z., Kiss, K., Jakab, G., Sipos, P., Belucz, B., & Németh, T. (2013). The use of UV-VIS-NIR
756 reflectance spectroscopy to identify iron minerals. *Astronomische Nachrichten*, 334(9), 940–943.

757 Torrent, J., & Barrón, V. (2002). Diffuse Reflectance Spectroscopy of Iron Oxides. *Encyclopedia of*
758 *Surface and Colloid Science*, 1.

759 Torrent, J., & Barrón, V. (2008). *Methods of Soil Analysis. Part 5. Mineralogical Methods*, Chapter
760 13 Diffuse Reflectance Spectroscopy, SSSA Book Series, No. 5. USA, 367–385.

761 Tositti, L., Brattich, E., Cinelli, G., & Baldacci, D. (2014). 12 years of ⁷Be and ²¹⁰Pb in Mt. Cimone,
762 and their correlation with meteorological parameters. *Atmospheric Environment*, 87, 108–122.
763 [https://doi.org/https://doi.org/10.1016/j.atmosenv.2014.01.014](https://doi.org/10.1016/j.atmosenv.2014.01.014)

764 Usher, C. R., Michel, A. E., & Grassian, V. H. (2003). Reactions on mineral dust. *Chemical Reviews*,
765 103(12), 4883–4940.

766 van den Berg, R., Hoefsloot, H., Westerhuis, J., Smilde, A., & van der Werf, M. (2006). Van den
767 Berg RA, Hoefsloot HCJ, Westerhuis JA, Smilde AK, Van der Werf MJ.. Centering, scaling, and
768 transformations: improving the biological information content of metabolomics data. *BMC Genomics*
769 7: 142-157. *BMC Genomics*, 7, 142. <https://doi.org/10.1186/1471-2164-7-142>

770 Waele, B. de, Aitken, A., Mourik, M. van, Laab Laab, K. O., Elhacen Ould Med Yeslem, M., &
771 Mohamedou, T. (2019). From a Mining Mindset to Regional Discovery: A Case Study for Hematite
772 Iron Ore Exploration in Mauritania. *ASEG Extended Abstracts*, 2019(1), 1–3.
773 <https://doi.org/10.1080/22020586.2019.12073145>

774 Ward, J. H. (1963). Hierarchical groupings to optimize an objective function. *J. Am. Stat. Assoc.*,
775 234–244.

776 Xu, J., DuBois, D., Pitchford, M., Green, M., & Etyemezian, V. (2006). Attribution of sulfate aerosols
777 in Federal Class I areas of the western United States based on trajectory regression analysis.

780

781 **FIGURE LEGENDS**

782 Figure 1. Map and location of Sierra Nevada sampling station.

783 Figure 2. Scheme of the integrating sphere, $0^\circ/d$ geometry. The UV-Vis incident light hits the sample
784 perpendicularly. Any specular component of reflection from the sample is excluded from
785 measurement since this component is directed out of the sphere through the transmittance sample
786 entrance port and, therefore, the detector only measures the diffuse reflectance component.

787 Figure 3. (a) Graphic representation of blank filter (B) and sampled filters (SN1, ...SN19) based on
788 chroma (C_{ab}^*) and hue (h_{ab}°). (b) Zoomed plot on sampled filters. The colors of three specific samples
789 (SN15, SN7, SN12) are shown.

790 Figure 4. Median and range of the UV-Vis absorption bands of some iron oxide minerals in the second
791 derivative of K-M function spectra, adapted from Torrent & Barrón, 2008. It can be seen that below
792 600 nm, there are three absorption bands at around 420, 480, and 535 nm.

793 Figure 5. Reflectance spectra (a), Savitzky-Golay second derivative of Kubelka-Munk (K-M)
794 function spectra (b), and baseline subtraction and quantification of relevant peak heights (c) for SN15
795 (grayish filter), SN7 (brownish filter), and SN12 (reddish filter).

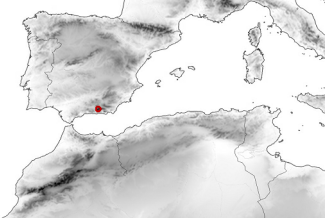
796 Figure 6. (a) Sample series of h_{480nm} (semi-quantitative data of several iron oxide minerals, mainly
797 goethite), h_{535nm} (semi-quantitative data of hematite), and elemental iron concentration (Fe). (b)
798 Scatter plots of h_{480nm} vs. Fe and h_{535nm} vs. Fe.

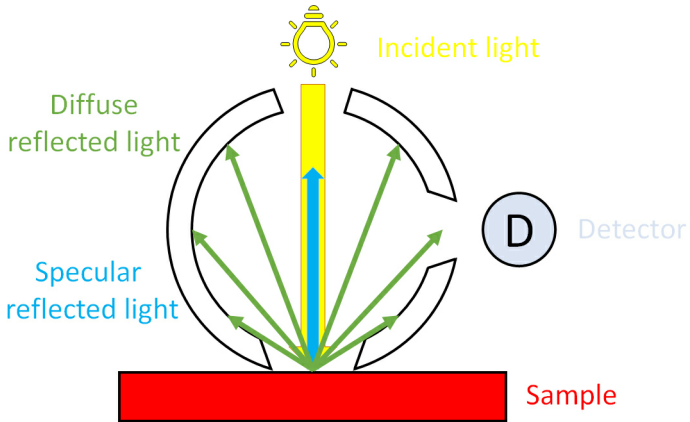
799 Figure 7. Dendrogram of Ward's hierarchical clustering method starting from CIELCH parameters
800 and semi-quantitative data of iron oxide minerals. The clustering solution with two clusters is
801 highlighted by squares.

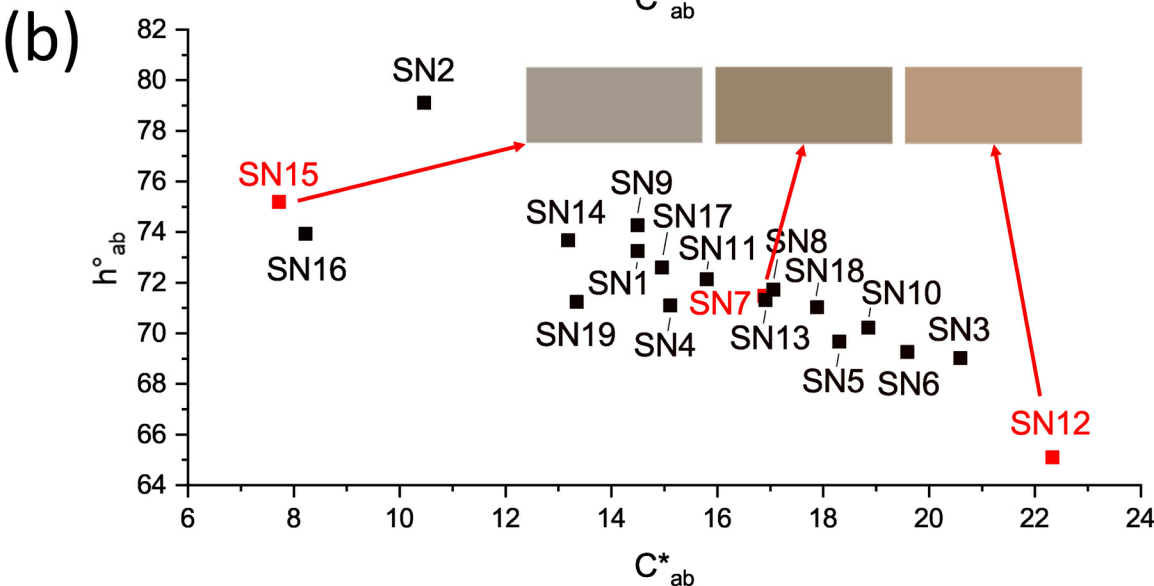
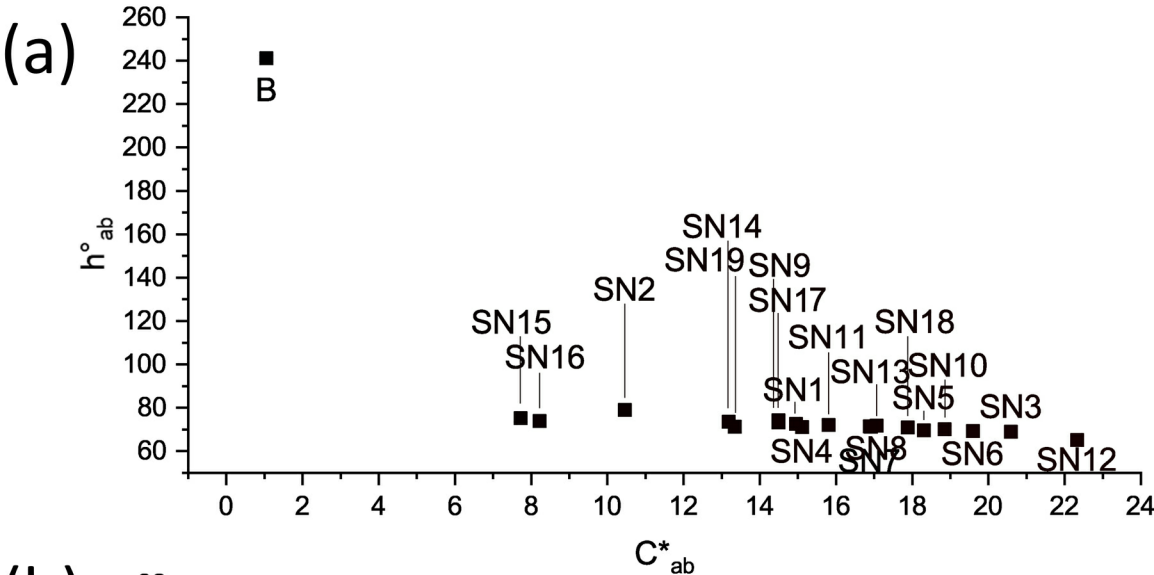
802 Figure 8. (a) Sample series of PM₁₀ data ($\mu\text{g}/\text{m}^3$) with the association of PM filters to the respective
803 clusters (cluster 1 and cluster 2). (b) Display of PM filters colors, look at subsection 3.1. (c) Sample
804 series of h_480nm (semi-quantitative data of several iron oxide minerals) and h_535nm (hematite),
805 look at subsection 3.2.

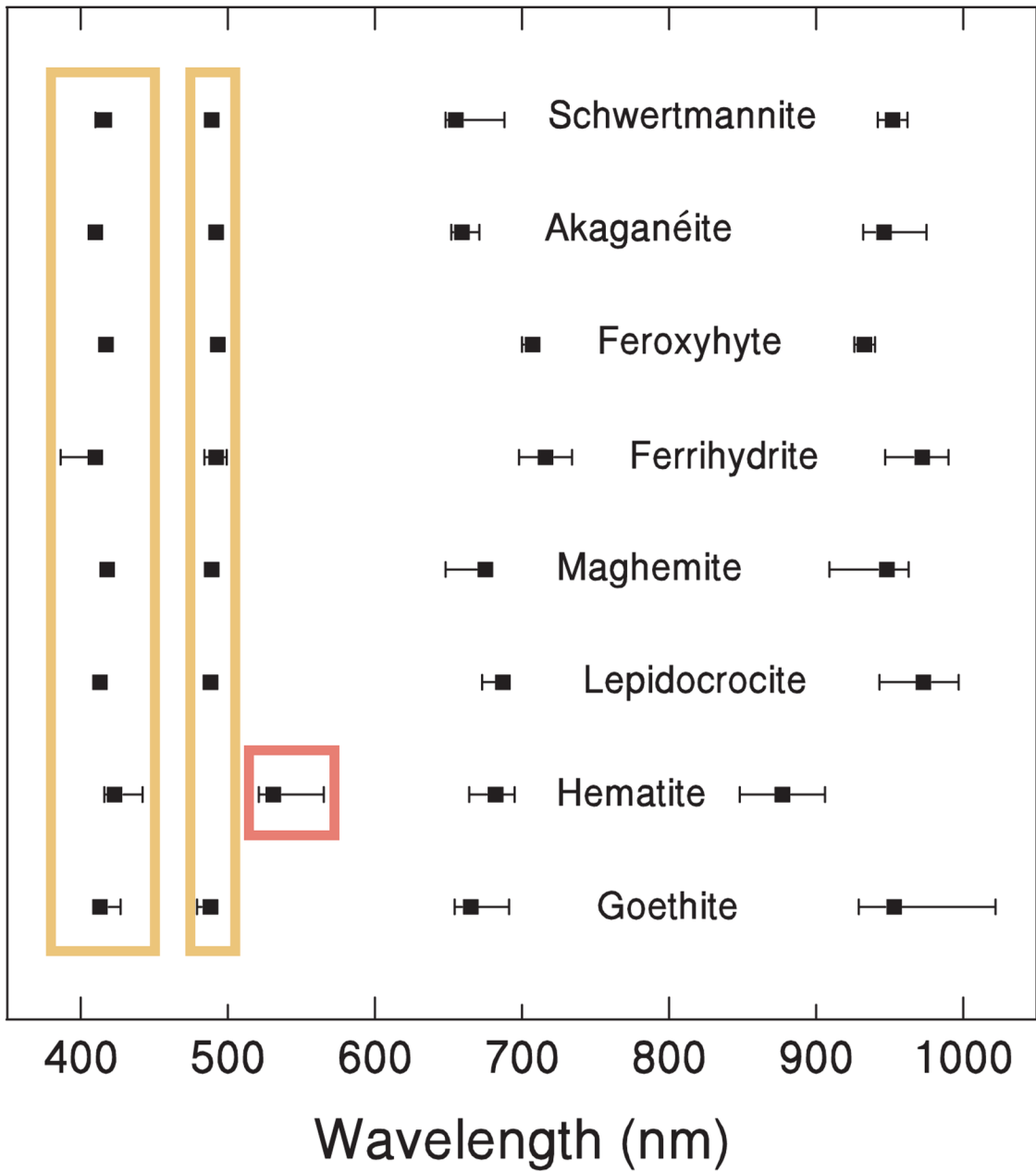
806 Figure 9. (a) Stacked bar chart of the percentage residence time over each examined region and PM
807 filter; Sample series of residence time over Mauritania (b) and the Atlantic Ocean, below 800 meters
808 (c).

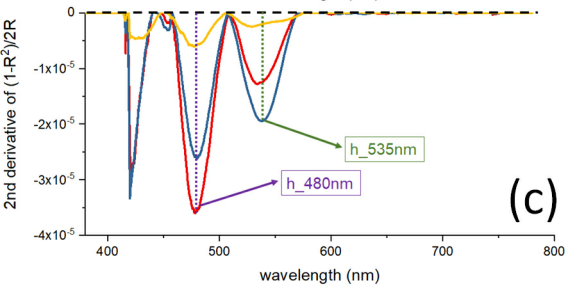
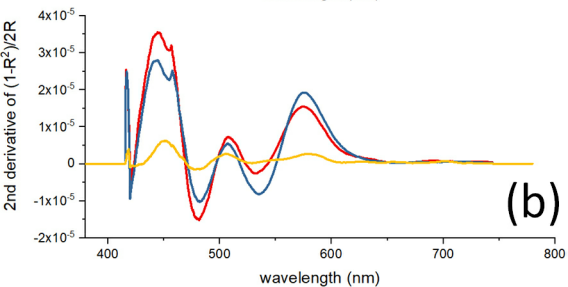
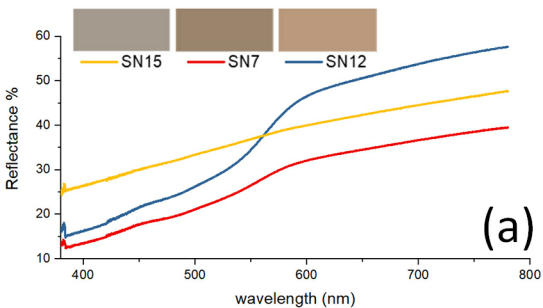
809 Figure 10. Corrected reflectance (True Color) Terra/MODIS snapshots for 4 June 2016 (a) and 5 June
810 2016 (b); Merged DT/DB Aerosol Optical Depth (Land and Ocean) Aqua/MODIS snapshots from 5
811 June 2016 (c) to 8 June 2016 (f). Higher AOD values are indicated by a more reddish color and allow
812 following the dust plume transport. The red square in a) and b) highlights the Chott el-Jerid Lake
813 (Tunisia) while the light blue star in c), d), e), and f) indicates the PM sampling station in Sierra
814 Nevada (37.096 N, -3.387 W, 2550 m a.s.l.). Images have been retrieved from the NASA EOSDIS,
815 worldview tool at <https://worldview.earthdata.nasa.gov>.

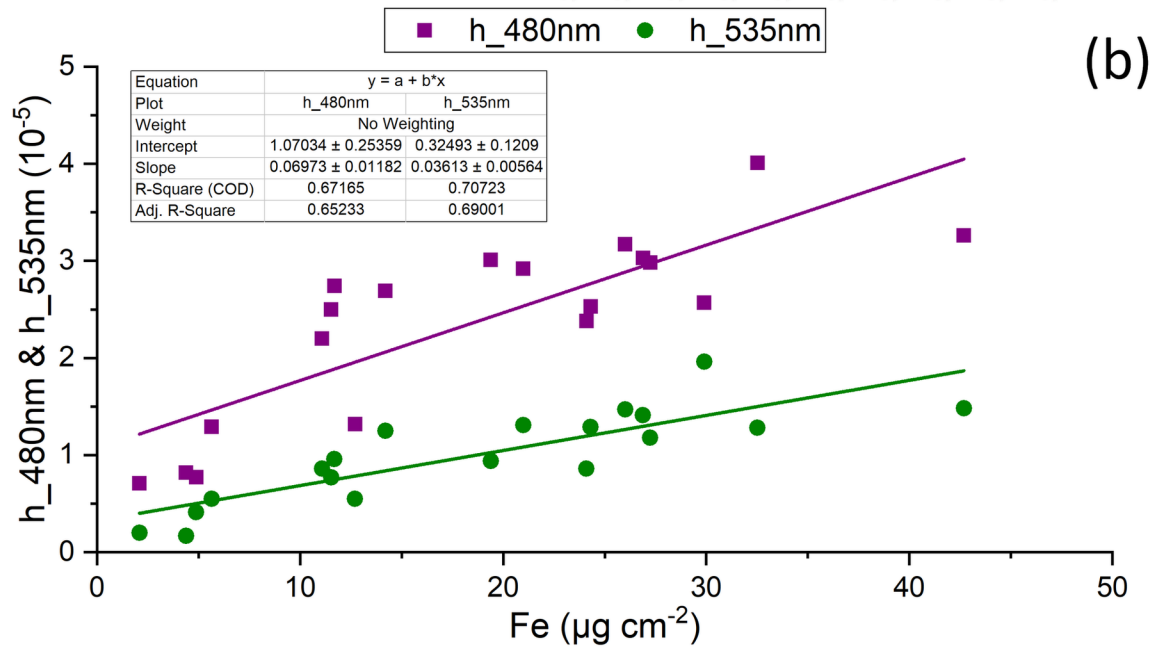
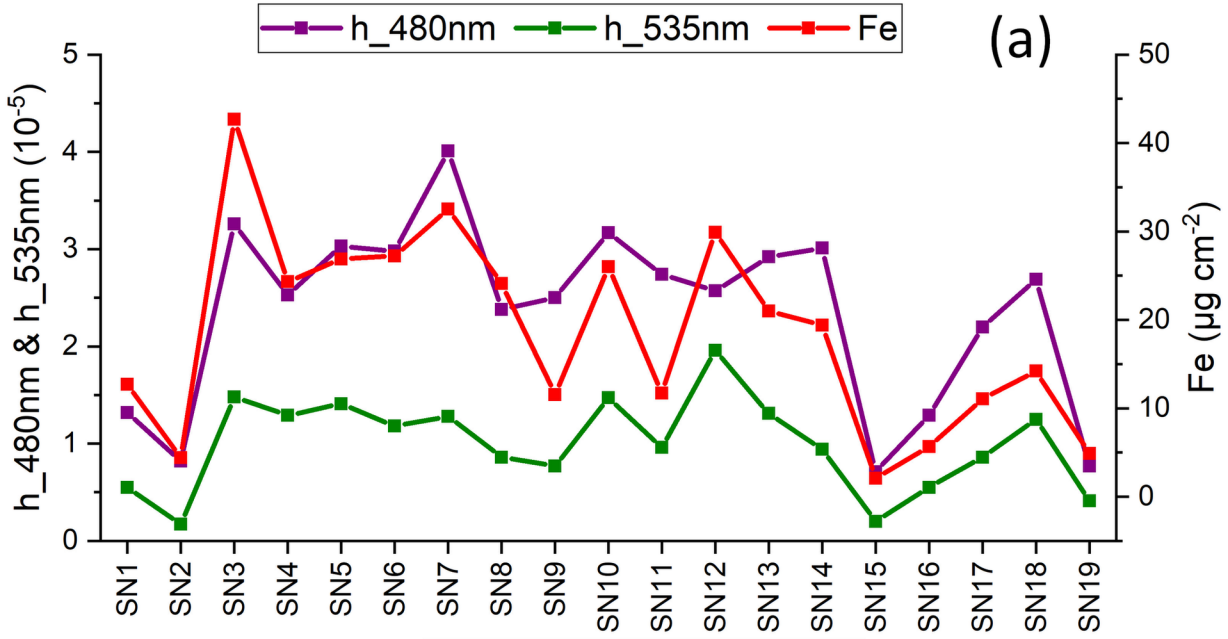


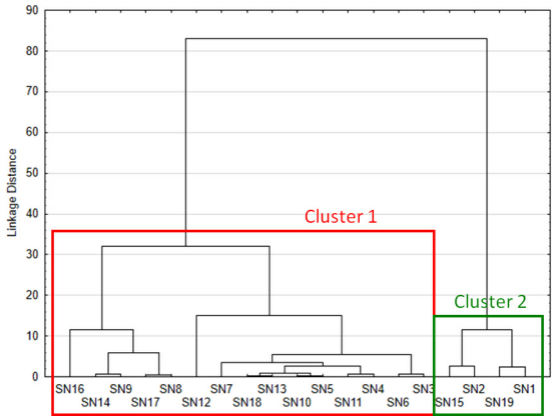


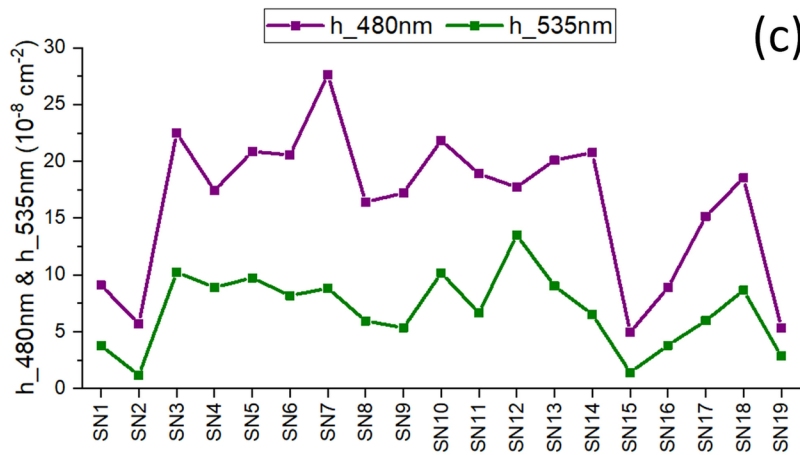
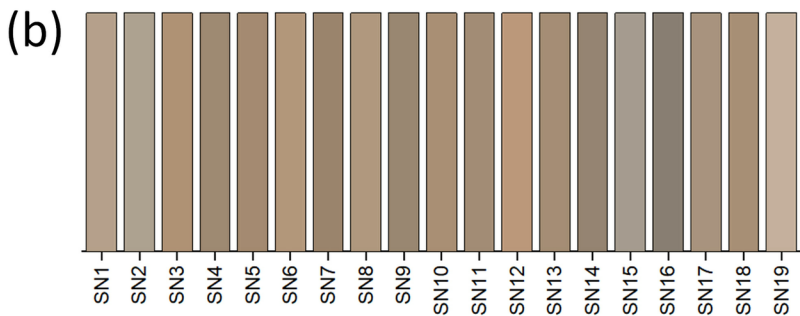
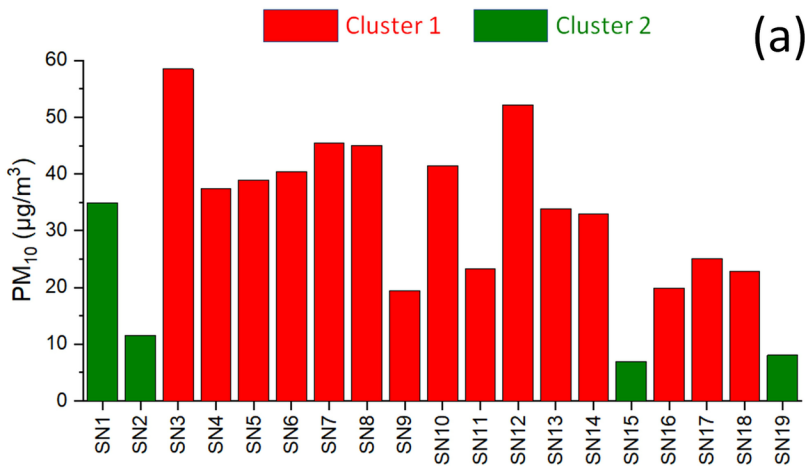


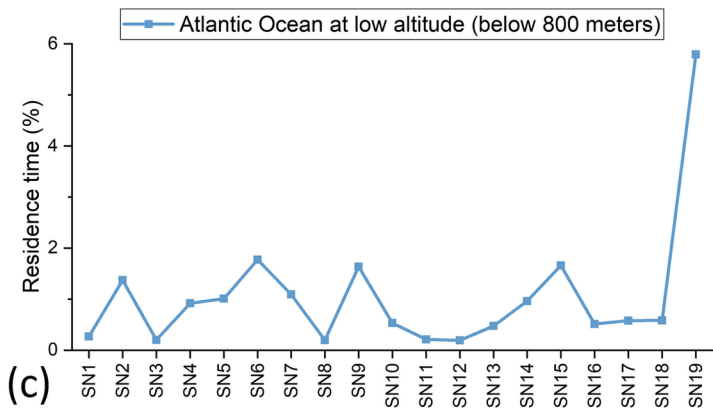
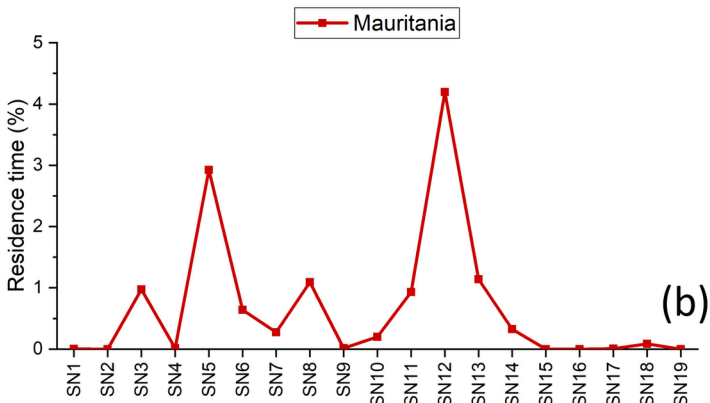
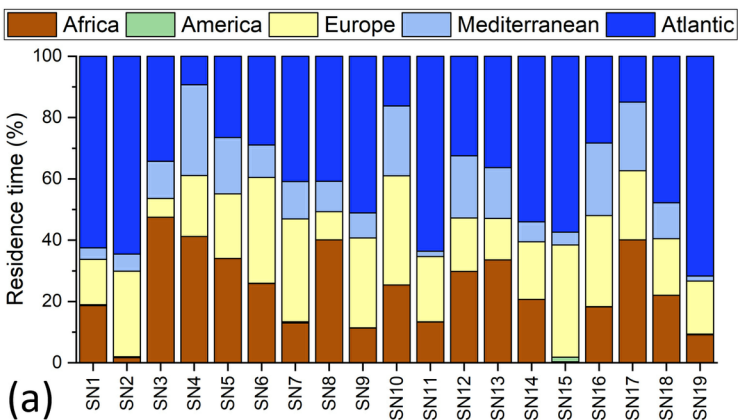












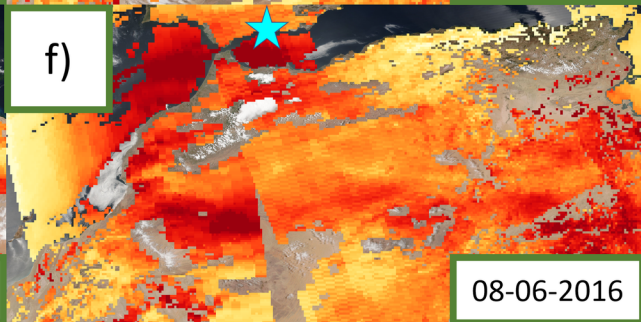
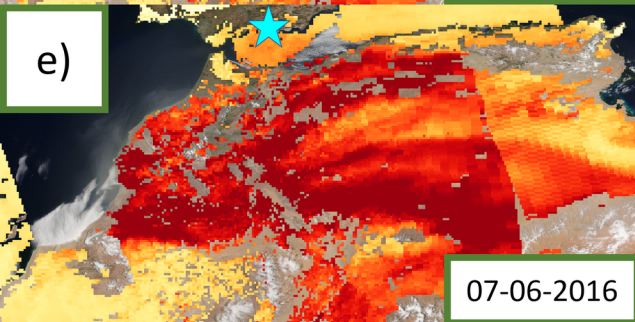
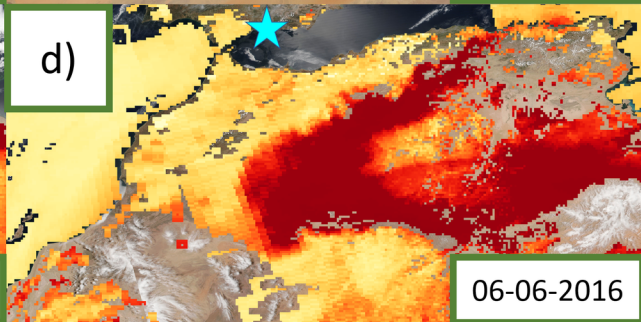
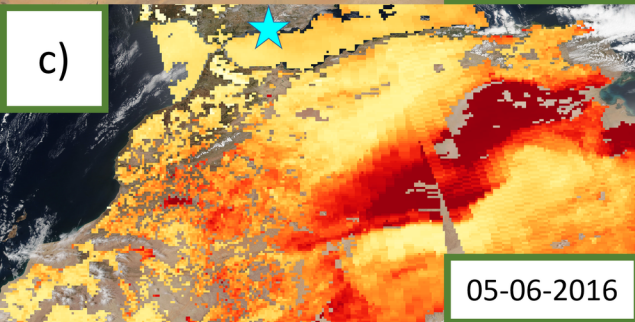
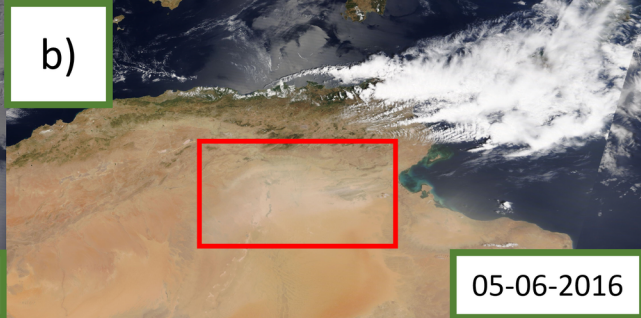
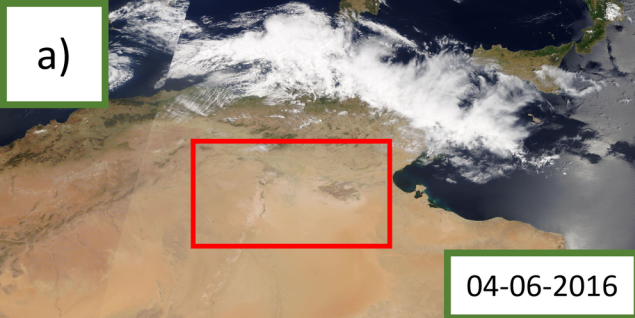


Table 1. Average values and standard deviations (numbers in brackets) of the colorimetric parameters for the analyzed samples. The colors obtained from the conversion to RGB color model by the online tool nix Color Sensor (<https://www.nixsensor.com/free-color-converter/>) are displayed in the last column of this table.





















Sample	L*	a*	b*	C _{ab} *	h _{ab} °	Color
B	95.46 (0.11)	-0.51 (0.05)	-0.92 (0.13)	1.05 (0.14)	241.15 (0.81)	
SN1	67.49 (2.68)	4.14 (1.19)	13.89 (4.42)	14.49 (4.57)	73.26 (0.64)	
SN2	66.85 (3.60)	1.99 (0.43)	10.27 (1.08)	10.46 (1.13)	79.11 (1.53)	
SN3	62.63 (3.07)	7.37 (0.56)	19.23 (1.36)	20.59 (1.47)	69.03 (0.11)	
SN4	58.53 (2.46)	4.86 (1.55)	14.31 (4.99)	15.11 (5.22)	71.10 (0.71)	
SN5	59.27 (2.79)	6.33 (0.09)	17.16 (1.64)	18.30 (1.56)	69.67 (1.66)	
SN6	64.43 (2.91)	6.84 (0.46)	18.35 (3.35)	19.59 (3.28)	69.27 (2.52)	
SN7	56.77 (2.12)	5.36 (0.39)	16.02 (1.22)	16.89 (1.28)	71.48 (0.14)	
SN8	64.35 (1.41)	5.37 (1.63)	16.20 (4.63)	17.06 (4.90)	71.72 (0.38)	
SN9	57.51 (3.59)	3.94 (0.51)	13.94 (1.26)	14.49 (1.35)	74.27 (0.70)	
SN10	61.20 (3.26)	6.41 (1.31)	17.72 (2.97)	18.85 (3.23)	70.22 (0.79)	
SN11	59.83 (3.63)	4.86 (0.81)	15.04 (2.11)	15.80 (2.25)	72.13 (0.89)	
SN12	65.59 (0.76)	9.41 (1.52)	20.24 (2.92)	22.33 (3.28)	65.11 (0.65)	
SN13	60.28 (3.57)	5.43 (0.80)	16.02 (1.76)	16.91 (1.93)	71.31 (0.78)	
SN14	56.44 (1.09)	3.72 (0.95)	12.65 (2.98)	13.18 (3.13)	73.68 (0.49)	
SN15	64.91 (2.89)	1.94 (0.32)	7.47 (1.86)	7.72 (1.88)	75.19 (1.56)	
SN16	53.75 (2.55)	2.25 (0.27)	7.90 (1.52)	8.22 (1.53)	73.93 (1.58)	
SN17	62.68 (2.65)	4.46 (0.53)	14.27 (2.03)	14.95 (2.09)	72.60 (0.90)	
SN18	61.01 (2.99)	5.80 (0.09)	16.91 (1.04)	17.88 (1.00)	71.04 (0.98)	
SN19	73.23 (2.41)	4.20 (0.56)	12.63 (2.16)	13.34 (1.97)	71.24 (4.53)	

Table 2. Average values and standard deviations (numbers in brackets) of the semi-quantitative data of mixed iron oxide minerals (h_480nm) and hematite (h_535 nm).

Sample	h_480nm (10⁻⁵)	h_530nm (10⁻⁵)
B	0.025 (0.009)	0.011 (0.005)
SN1	1.32 (0.37)	0.55 (0.08)
SN2	0.83 (0.16)	0.17 (0.04)
SN3	3.27 (0.71)	1.49 (0.20)
SN4	2.53 (1.20)	1.29 (0.17)
SN5	3.03 (0.03)	1.42 (0.06)
SN6	2.99 (0.27)	1.19 (0.19)
SN7	4.01 (0.38)	1.28 (0.11)
SN8	2.38 (0.90)	0.87 (0.08)
SN9	2.50 (0.05)	0.78 (0.16)
SN10	3.17 (0.11)	1.48 (0.09)
SN11	2.74 (0.10)	0.97 (0.18)
SN12	2.57 (0.10)	1.96 (0.22)
SN13	2.92 (0.62)	1.31 (0.33)
SN14	3.02 (0.64)	0.95 (0.15)
SN15	0.72 (0.46)	0.21 (0.13)
SN16	1.29 (0.15)	0.55 (0.26)
SN17	2.20 (0.06)	0.87 (0.19)
SN18	2.69 (0.52)	1.26 (0.31)
SN19	0.78 (0.18)	0.41 (0.09)

Table 3. Spearman correlation coefficients obtained for each pair of variables. L* = CIELAB lightness, C_{ab}* = CIELAB chroma, h_{ab}[°] = CIELAB hue, Fe = elemental iron, PM₁₀ = particulate matter, h_480nm = semi-quantitative data of mixed iron oxide minerals, h_535nm= semi-quantitative data of hematite.

	L*	C _{ab} *	h _{ab} [°]	Fe	PM ₁₀	h_480nm	h_535nm
L*	1.00						
C _{ab} *	0.08	1.00					
h _{ab} [°]	-0.11	-0.90	1.00				
Fe	-0.20	0.85	-0.80	1.00			
PM ₁₀	-0.11	0.81	-0.74	0.96	1.00		
h_480nm	-0.47	0.69	-0.60	0.84	0.75	1.00	
h_535nm	-0.28	0.85	-0.83	0.86	0.81	0.81	1.00



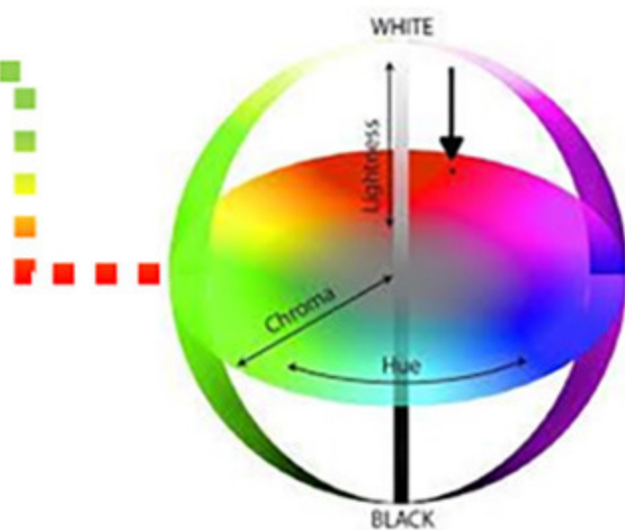
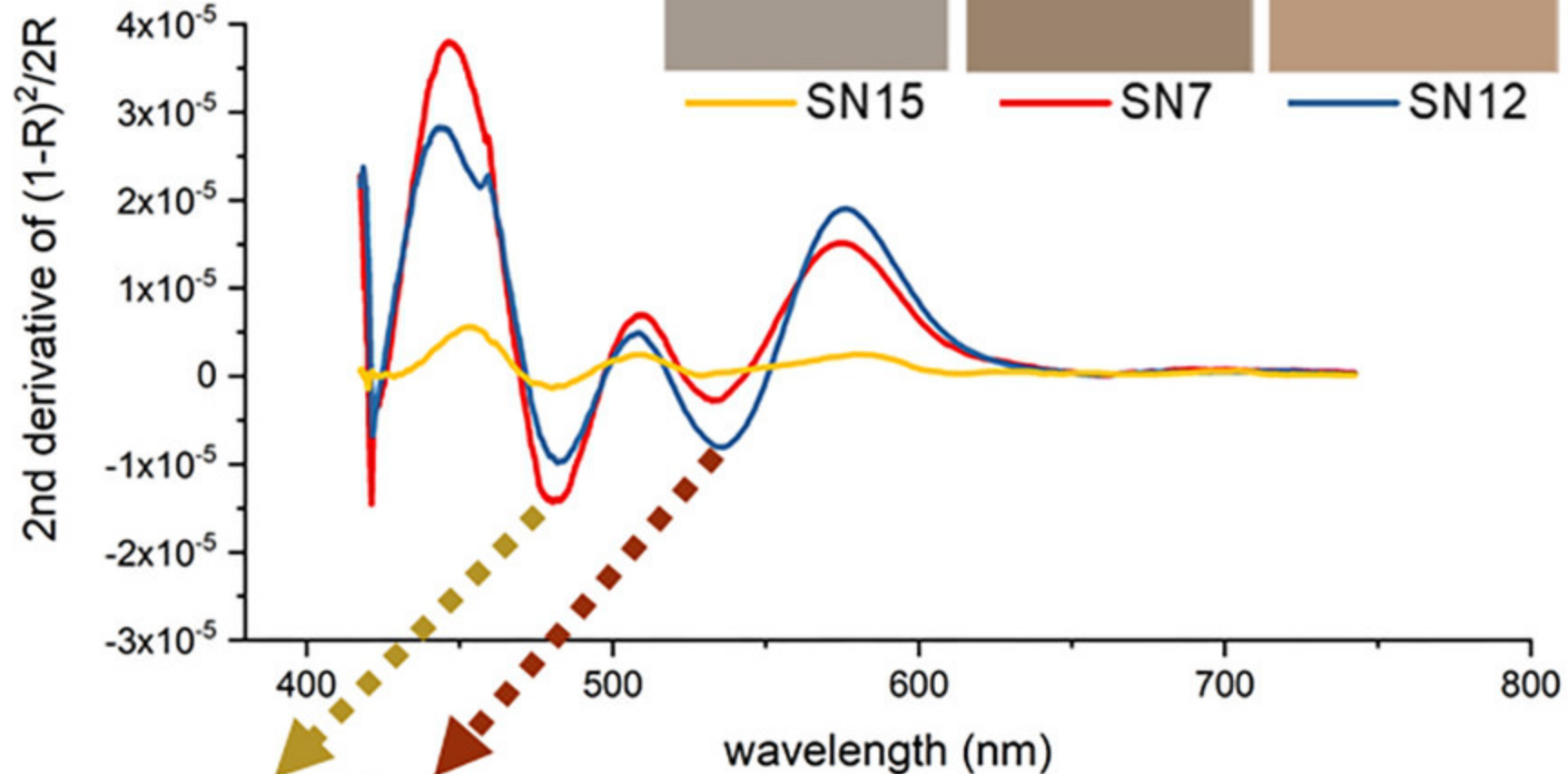
SN15

SN7

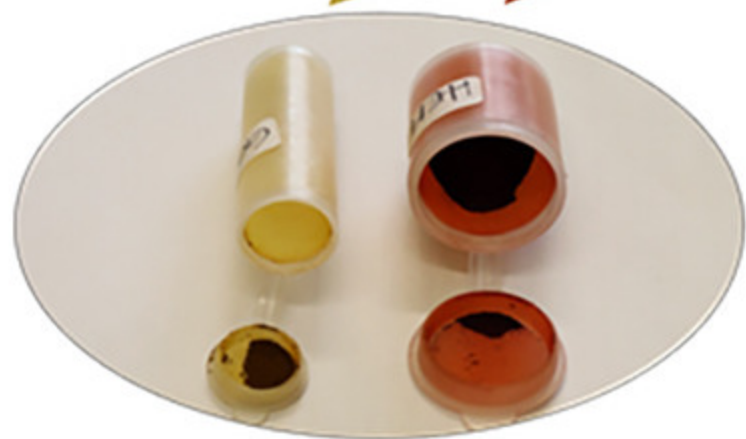
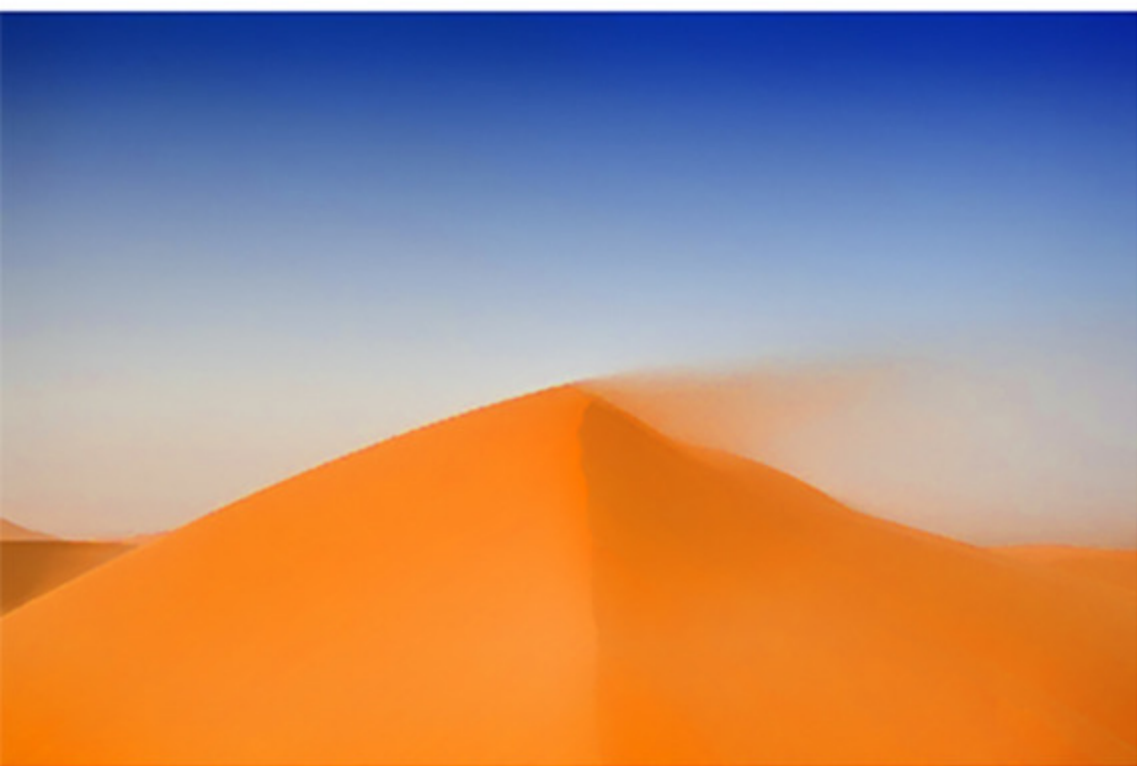
SN12



UV-Vis
DRS



CIE LCH



GOETHITE

HEMATITE

